Title

Magnetotelluric Imaging of the Lithospheric Structure of the Southern Oklahoma Aulacogen: Evidence for Long-Term Weakening Caused by Rifting

Journal

Journal of Geophysical Research: Solid Earth, 128(6)

ISSN

2169-9313

Authors

Chase, BFW
Unsworth, MJ
Atekwana, EA
et al.

Publication Date

2023-06-01

DOI

10.1029/2023jb026555

Peer reviewed

JGR Solid Earth

RESEARCH ARTICLE
10.1029/2023JB026555

Magnetotelluric Imaging of the Lithospheric Structure of the Southern Oklahoma Aulacogen: Evidence for Long-Term Weakening Caused by Rifting

B. F. W. Chase[1], M. J. Unsworth[1], E. A. Atekwana[2], R. L. Evans[3], and J. Zhu[3]

[1]Department of Physics, University of Alberta, Edmonton, AB, Canada, [2]Department of Earth and Planetary Sciences, University of California Davis, Davis, CA, USA, [3]Woods Hole Oceanographic Institution, Falmouth, MA, USA

Key Points:

- A 2-D magnetotelluric model of the Southern Oklahoma Aulacogen in the USA is compared with regional geochemical and mineral physics data
- After rifting, an enriched plume may have been accreted to the lithosphere and increased the lithospheric thickness to its current value
- Metasomatism during rifting rheologically weakened the lithosphere, allowing deformation during the Ancestral Rocky Mountain orogeny

Supporting Information:

Supporting Information may be found in the online version of this article.

Correspondence to:

B. F. W. Chase,
bchase1@ualberta.ca

Citation:

Chase, B. F. W., Unsworth, M. J., Atekwana, E. A., Evans, R. L., & Zhu, J. (2023). Magnetotelluric imaging of the lithospheric structure of the Southern Oklahoma Aulacogen: Evidence for long-term weakening caused by rifting. *Journal of Geophysical Research: Solid Earth*, *128*, e2023JB026555. https://doi.org/10.1029/2023JB026555

Received 14 FEB 2023
Accepted 6 JUN 2023

Author Contributions:

Conceptualization: B. F. W. Chase, E. A. Atekwana
Formal analysis: B. F. W. Chase, M. J. Unsworth, E. A. Atekwana, R. L. Evans, J. Zhu
Funding acquisition: B. F. W. Chase, E. A. Atekwana
Investigation: B. F. W. Chase, E. A. Atekwana
Methodology: B. F. W. Chase, M. J. Unsworth, E. A. Atekwana
Project Administration: E. A. Atekwana

Abstract Magnetotelluric data were used to study the lithosphere structure of the Southern Oklahoma Aulacogen (SOA). Inversion of the data revealed two low resistivity anomalies beneath the SOA. The first is located in the depth range 0–90 km in the crust and upper lithospheric mantle. The second extends from a depth 100 km to the base of the lithospheric mantle and extends away from the SOA to the ends of the profile. The cause of low resistivity anomalies is discussed in relation to the tectonic evolution of the region and recent laboratory experiments on rock conductivity. The first anomaly is attributed to the combination of (a) water present in mantle minerals and (b) the formation of hydrous mineral phases by interactions between a plume and the lithosphere during rifting. Grain size reduction and fabric alignment from deformation during the Ancestral Rocky Mountain (ARM) orogeny may have also contributed to the low resistivity. This enrichment phase may have mechanically weakened the lithosphere and allowed deformation to occur during the ARM orogeny. The low resistivity of the deeper anomaly is attributed to a fluorine-enriched phlogopite layer that is also coincident with an observed seismic mid-lithosphere discontinuity (MLD). A lithosphere keel of mantle minerals enriched in water underlies this layer and may have formed by accretion of the plume head to the lower lithosphere after rifting, which also rethickened the lithosphere to its present-day depths. The MLD may then reflect a melt layer along a paleo lithosphere-asthenosphere boundary entombed during the accretion.

Plain Language Summary Earth's tectonic plates result from modification by past and present tectonic processes such as rifting and plumes. Processes that occurred in the past can be understood by present day studies of these processes that are active today. Geophysical imaging is a key part of these investigations as it provides information about subsurface structure. One method that is widely used is magnetotellurics (MT) which provides information about electrical resistivity. This parameter is sensitive to the presence of fluids and past metamorphism. The Southern Oklahoma Aulacogen is a failed rift located in the central USA. After the rifting occurred, compression formed the Ancestral Rocky Mountains (ARMs). This study uses MT data to understand how past tectonic events modified the North American Plate in this region. The results show that the lithosphere beneath the rift has a low electrical resistivity relative to the surrounding region. This suggests that metamorphism changed the composition of lithosphere and made it weaker. When later tectonic events caused compression, this weakening allowed the ARM to form. These results help us to understand how rifts and plumes modify plates at the present.

1. Introduction

Cratonic regions are areas characterized by long-term lithospheric stability that often persists through a significant amount of earth history. However, many studies have shown that cratons can be modified by later tectonic events and in some cases destroyed (e.g., Abdelsalam et al., 2002; Liu et al., 2021; Tang et al., 2013). The study of the deep lithosphere beneath and along craton margins offers the opportunity to understand the processes that can modify and potentially destroy cratons, and to connect these processes with evolution of the lithosphere on the regional scale. This type of study can also offer constraints on volatile fluxes and storage, rheology, and long-term survivability of the subcontinental lithosphere mantle (SCLM), as well as the formation of economically significant mineral deposits within the cratonic lithosphere (Aulbach, 2018; S. F. Foley & Fischer, 2017; Frezzotti & Ferrando, 2018; Griffin et al., 2013; O'Reilly & Griffin, 2013; Selway, 2018).

The southern midcontinent of the United States is located on the margin of the Laurentian craton. This region records geologic events that extend from the initial assembly of Laurentia to its breakup from Pangea. Many of

Resources: B. F. W. Chase, M. J. Unsworth, E. A. Atekwana
Software: B. F. W. Chase, M. J. Unsworth, R. L. Evans, J. Zhu
Supervision: M. J. Unsworth, E. A. Atekwana, R. L. Evans
Validation: B. F. W. Chase, E. A. Atekwana, R. L. Evans
Visualization: B. F. W. Chase
Writing – original draft: B. F. W. Chase, M. J. Unsworth, E. A. Atekwana, R. L. Evans
Writing – review & editing: B. F. W. Chase, M. J. Unsworth, E. A. Atekwana, R. L. Evans

these features have escaped later tectonic reworking, offering a valuable window into the evolution of the continent. Since the breakup of Pangea, regional tectonic activity has ceased, and Phanerozoic sedimentary rocks up to 12 km thick have covered most of the region. This has complicated investigation of regional basement rocks critical for tectonic studies, making geophysical imaging necessary. Notably, the EarthScope seismic array has defined variations in seismic velocity, Moho depths, lithosphere structure, and the lithosphere-asthenosphere boundary (LAB), offering valuable insights into regional terrane assembly and tectonic evolution, as well as how these processes modified and are preserved in the lithosphere (e.g., Kumar et al., 2012; Nyamwandha et al., 2016; Shen et al., 2013). The complimentary EarthScope magnetotellurics (MT) array has offered additional insights by defining regions of lithosphere enrichment and modification resulting from regional tectonic processes (e.g., Bedrosian, 2016; DeLucia et al., 2019; Yang et al., 2015).

This paper presents an investigation of the Southern Oklahoma Aulacogen (SOA), which is a failed, structurally inverted rift located in Oklahoma and Texas (Figure 1). The SOA was involved in two episodes of Laurentian evolution. The first was as a failed rift arm during the Cambrian breakup of Rodinia, and the second was as an uplift in the Pennsylvanian-Permian Ancestral Rocky Mountain (ARM) orogeny during the assembly of Pangea (Kluth & Coney, 1981; Leary et al., 2017; Whitmeyer & Karlstrom, 2007). Study of the SOA provides the opportunity to understand (a) how Cambrian rifting modified the lithosphere, (b) if this modification is still preserved, and (c) how this modification may have influenced the evolution of the SOA during the ARM orogeny. Relative to the much of the regional basement the SOA is buried at shallow depths (100s of meters to <1 km) which has allowed it to be subjected to a wide variety of geochemical, geophysical, and structural studies (e.g., Brewer et al., 1983; Chase et al., 2022; Hanson et al., 2013). However, geophysical imaging of sufficient resolution at depths greater than the mid-crust is lacking. Further, while the EarthScope seismic array extended over the region the resolution is limited due to the large 70 km site spacing (Evanzia et al., 2014). The EarthScope MT array did not extend to the region.

In this paper, the first modern MT study of the SOA itself is described. The only other MT data in the region was a study of the adjacent Anadarko basin (Vozoff, 1972). A profile of 13 long period MT stations was collected from 2018 to 2019 and inverted to give a two-dimensional (2D) lithosphere-scale resistivity model. Details of the resistivity model are discussed to investigate the cause of the low resistivity zones observed and relate them to past tectonic processes. The implications of the electrical resistivity structure in relation to the evolution of Laurentia, particularly how they may relate to ARM tectonics and Rodinian rifting are discussed. It should be noted that the terms resistivity and conductivity, mathematical inverses of each other, are both used in this paper.

2. Geologic and Tectonic Framework

2.1. Geologic and Tectonic History

The SOA is located on the inferred terrane boundary between the Mazatzal and Granite-Rhyolite provinces (Whitmeyer & Karlstrom, 2007) (inset, Figure 1). Following terrane collision in the mid-Proterozoic, widespread granitoid intrusion occurred across both terranes around ∼1.4 Ga (Whitmeyer & Karlstrom, 2007). After this, there is no recorded activity until the early Cambrian during the breakup of Rodinia when the region rifted as the failed arm of a plume-driven rift-rift-rift triple junction centered near the present-day Oklahoma-Texas border (Hoffman et al., 1974; inset Figure 1). The original suture between the two terranes may have been a region of pre-existing weakness that aided rifting localization and development (Budnik, 1986; Keller & Stephenson, 2007; Yuan et al., 2014). An alternate interpretation was proposed by Thomas (2011, 2014), who suggested that the SOA was a leaky transform fault that is associated with pronounced lateral offset. This interpretation and rifting are not mutually exclusive (Hanson et al., 2013), but generally leaky transforms do not exhibit the extensive magmatism and produce magmas of different composition that are observed in the SOA (Brueseke et al., 2016; Skulski et al., 1991, 1992). Based on this analysis, the SOA is referred to as a rift in this paper.

Initial volcanism during rifting was mafic, of largely subalkaline tholeiitic affinity with another, smaller component of alkaline-transitional affinity, and produced the extensive Glen Mountain Layered Complex, gabbros, and ultramafic rocks at depth (Brueseke et al., 2016; Powell & Phelps, 1977). A later felsic stage emplaced mostly fluorine-rich, water-poor A-type magmas between and on top of the mafic units (Hanson et al., 2013; Hogan & Gilbert, 1998; Price, 2014). Numerous diabase dikes and sills intruding all other units were emplaced throughout rifting and mark the final stage of volcanism (Gilbert, 1983; Hanson et al., 2013). Some intermediate igneous

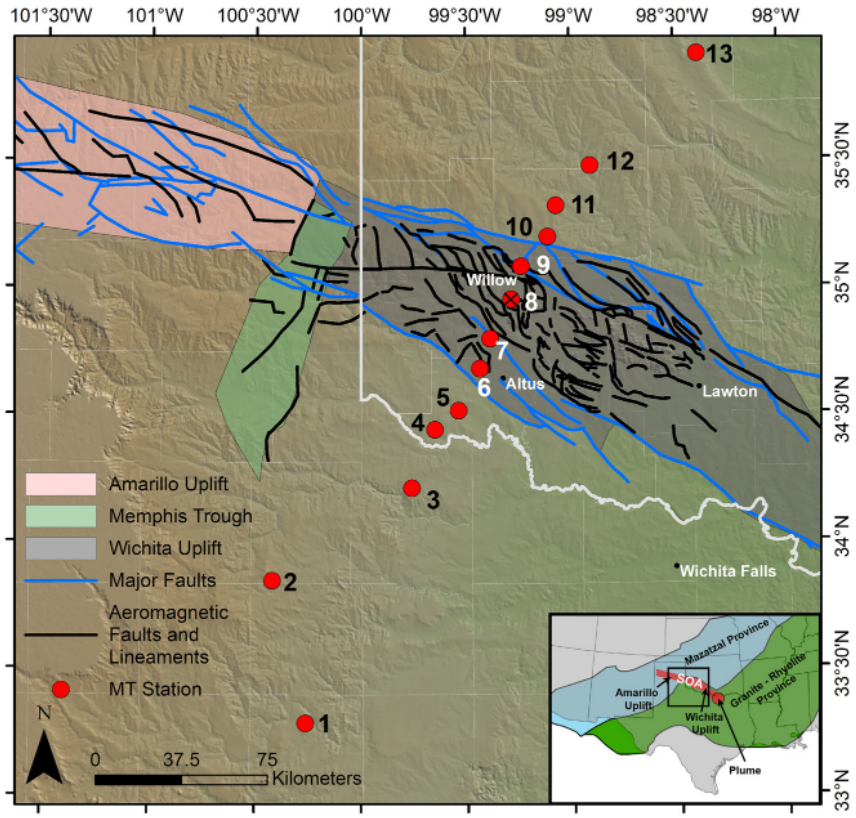

Figure 1. Map of the Southern Oklahoma Aulacogen in Oklahoma and Texas, where it breaks down into locally named uplifts (see inset). The station, station 8, with the black X was ultimately removed from the final inversion model. See text for details. Major faults from Marsh and Holland (2016). Aeromagnetic faults and lineaments from Chase et al. (2022). Tectonic terranes in the inset are from Whitmeyer and Karlstrom (2007).

rocks occur in the subsurface, with these units often intercalated with the rhyolitic units (Hanson et al., 2013). No calderas or volcanic centers have been reported, and feeder dikes are inferred to have produced most of the volcanism (McConnell & Gilbert, 1990), which can be defined in aeromagnetic data (Chase et al., 2022). Volcanism lasted from 539 to 529 Mya, was largely bimodal with limited breaks between phases, and most of the magmatism occurred in a ∼2 My timeframe from 532 to 530 Mya (Hogan & Gilbert, 1998; Wall et al., 2021). Geochemistry results point to (a) the derivation of felsic magmas by the partial melting of plume-derived mafic units or of a mafic underplate, (b) the derivation of mafic units from a plume of ocean island basalt (OIB) affinity, and (c) most units appear to have been generated with limited interaction and partial melting of the existing lithosphere (Brueseke et al., 2016; Hanson et al., 2013; Price, 2014; Wall et al., 2021). The total volume of igneous rock emplaced by the SOA was estimated by Hanson et al. (2013) to be at >250,000 km^3, which led the authors to argue the SOA was a Large Igneous Province, the only one reported along the southern margin of Rodinia during the Cambrian.

After rifting, the SOA experienced subsidence, with tectonic activity limited to pulses of broad crustal flexure from the Ordovician to the Devonian, occurring at the same time as the deposition of ∼4–5 km of sedimentary rock (Amsden, 1982; Gilbert, 1983). During the assembly of Pangea in the Pennsylvanian, the SOA was the first block to be uplifted as part of the larger ARM orogeny that occurred from Oklahoma to Colorado and New Mexico (Leary et al., 2017). Deformation in the SOA occurred in two phases. The first saw compressional NE-SW-directed stresses and a small amount of sinistral strike-slip movement, leading to structural inversion via thrust faulting. The first phase and thrust faulting ceased by the Atokan (∼311–308 Ma). A second phase, dominated by sinistral strike-slip movement, continued until sometime into the Permian (Brewer et al., 1983; Chase et al., 2022; Granath, 1989; Turko & Mitra, 2021). Overall, transpressional tectonics was the primary mechanism for SOA ARM deformation which resulted in ∼12–15 km of vertical uplift, ∼15 ± 5 km of crustal shortening, and sinistral strike slip deformation ranging from <1 km to as much as 40 km (Chase et al., 2022;

Granath, 1989; Keller & Stephenson, 2007; McConnell, 1989; Perry, 1989; Turko & Mitra, 2021). Continued sedimentary deposition would occur in the newly created basins yielding the 12–15 km deep Anadarko and 2–4 km deep Holis-Hardeman basins to the north and south of the SOA, respectively. The SOA has been tectonically inactive since the ARM but is a notable intraplate-seismic hazard capable of producing earthquake up to M_w 7.0 (Hornsby et al., 2020 and references therein).

2.2. Prior Geophysical Studies

Several geophysical surveys have studied the SOA, revealing that the upper to mid crust contains an extensive, high-density volcanic package (e.g., Chang et al., 1989; Keller & Baldridge, 2006). However, few surveys have imaged to depths greater than 15–25 km. The EarthScope seismic array is the only exception and revealed several seismic anomalies in the SCLM. These include a 2%–4% slow shear wave velocity anomaly at depths >75 km (Evanzia et al., 2014), a seismic mid-lithosphere discontinuity (MLD) at depths of 100–120 km (Kumar et al., 2012), and a southwest-dipping, high-angle slow seismic anomaly extending deep into the upper mantle (Netto & Pulliam, 2020). Other anomalies present are as follow. The first is a lithosphere-scale negative radial anisotropy anomaly interpreted as a terrain boundary (Yuan et al., 2014). The next is a velocity anomaly interpreted similarly as evidence of a paleo-suture terrane boundary zone (Porritt et al., 2014). There is a final seismic anisotropy anomaly with the fast direction parallel to the SOA that was interpreted as relict lithosphere fabrics or dikes (Comiskey, 2013; Refayee et al., 2014). In the crust, the products of SOA magmatism have been studied by the analysis of gravity data, which detected both a dense core of mafic units that extend downward into the mid-crust and the Moho at a depth of 40–45 km, deepening beneath the rift itself (Keller & Stephenson, 2007; Tave, 2013). Aeromagnetic data have revealed that the SOA is heavily deformed, with numerous NW to EW oriented faults (Chase et al., 2022). Additional geophysical data that is sensitive to the entire lithosphere and has closer site spacing to improve resolution are necessary to improve upon these prior observations and constrain the lithospheric structure of the SOA. Long-period MT data are suitable for this given their sensitivity to the entire lithosphere and to the presence of various electrically conductive mantle phases associated with tectonic modification (e.g., Bedrosian, 2016; DeLucia et al., 2019).

3. Data Analysis

3.1. Magnetotelluric Data Collection

From 2017 to 2019 long-period MT stations were collected at 13 stations along a NE-SW striking profile oriented perpendicular to the N60°W strike of the SOA (Figure 1). Stations were spaced ∼20 km within the SOA and recorded data for 2–3 weeks. The three stations outside of the rift were spaced at ∼50 km and recorded data for 6 weeks (Figure 1). Data were collected with LEMI-417M instruments using a fluxgate magnetometer and non-polarizable silver chloride electrodes. Reliable transfer functions were obtained at 26 periods in the range of 4–25,000 s using the bounded influence code, BIRRP (Chave & Thomson, 2004). Time series data at each site were remote referenced to other synchronously recording sites to remove noise and improve data quality. The resulting apparent resistivity and phase curves for all sites are included in Figure S1 in Supporting Information S1 and show low resistivity values at short periods, high resistivity values at mid periods, and a final trend toward low resistivity values at long periods.

3.2. Dimensionality of Data

The dimensionality of the data was evaluated using the induction vectors and phase tensors. Induction vectors are computed from the vertical and horizontal components of the magnetic field and in the convention of Parkinson (1959) point to concentrations of currents (i.e., conductive zones). The phase tensor displays the azimuthal variation of the impedance and gives a graphical way to determine if the subsurface has a 1-D, 2-D, or 3-D resistivity structure (Caldwell et al., 2004). The direction of the major axis is either parallel or perpendicular to the geoelectric strike. A parameter called the skew angle is also calculated and indicates the dimensionality (Booker, 2014). A circular phase tensor with zero skew reflects 1-D resistivity structure, an elliptical tensor with zero skew indicates 2-D resistivity structure, and an elliptical tensor with non-zero skew indicates 3-D resistivity structure (Booker, 2014; Caldwell et al., 2004). An important aspect of the phase tensor is that it is not affected by near surface galvanic distortions (Booker, 2014).

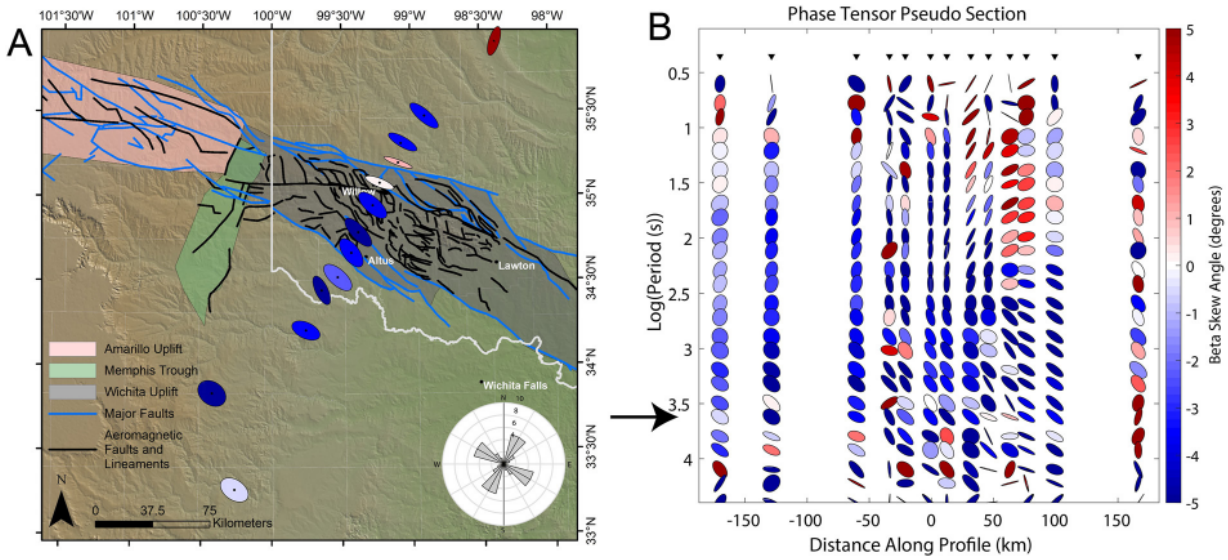

Figure 2. (a) Phase tensors and induction vector map of the stations over the Southern Oklahoma Aulacogen (SOA) (red and gray polygons) at 4,000 s, where the geoelectic strike of the SOA is most obvious. The rose diagram in the lower right show the orientations of the phase tensors in gray. (b) Phase tensors plot showing the dimensionality of the data as a function of period.

Information about dimensionality comes from both the induction vectors and phase tensors. The phase tensors exhibit significantly 3-D behavior at the three periods less than 10 s with (a) skew angles ranging from 5° to −5° and (b) scattered ellipse orientations (Figure 2b). This is likely due to the complexity of the conductivity structure associated with the Anadarko and Holis-Hardeman sedimentary basins. Deeper resistivity structure is sensed by longer periods. At periods greater than 400 s, the phase tensor axes align in a direction ∼N60°W, roughly parallel to the strike of the SOA, and exhibit more 2-D behavior with skew values ranging from −3° to 2° (Figure 2). This suggests a conductive feature is located beneath the SOA. The induction vectors at the same period as Figure 2 are shown in Figure S2 in Supporting Information S1 and also indicate a geoelectric strike parallel to the SOA.

Since this study is focused on the deep lithosphere structure of the SOA the first three periods were removed to simplify the inversion. This left the data at 23 periods over a range of 12–25,000 s for inversion. The longest three periods also show the possible influence of 3-D effects. An inversion was undertaken with these periods excluded and the resulting model was very similar to the one shown in Figure 4a. The N60°W orientation of the phase tensor provides an estimate of the geoelectric strike direction necessary for 2-D inversion, so the data was rotated to this orientation. The pseudosections in Figure 3a display the transverse electric (TE) and transverse magnetic (TM) modes for the data and inversion model. The TE mode is computed from electric currents flowing along strike of the SOA and the physics is dominated by inductive effects, making it good at detecting conductors. The TM mode is computed from currents flowing across strike and includes both inductive and galvanic effects, making it capable of detecting more moderate conductors and resistors. At the shortest periods along the entire profile low apparent resistivity values are observed in both modes, reflecting the presence of low resistivity sedimentary rocks at the surface. At periods greater than 100 s the apparent resistivity and phase vary along the profile in both modes, indicating a 2-D structure for the crystalline basement. There is a marked change in both the TE and TM modes at ∼200 km along the profile, coincident with the SOA. Here, the TM mode detects the SOA as a region of slightly higher apparent resistivity values relative to the low resistivity of the surrounding region. The TE mode has a similar apparent resistivity response, but the phase data at the SOA is slightly elevated at mid periods, indicating the presence of a conductor in the region.

3.3. Inversion of MT Data

The data were inverted using the 2-D isotropic non-linear conjugate gradient code of Rodi and Mackie (2001) to produce a 2-D resistivity model. A 3-D modeling approach was not used due to the 2-D survey geometry and because preliminary 3-D inversions showed they were biased to the initial starting model. Error floors of 20% and 5% were applied to the apparent resistivity and phase data, respectively. To account for static shifts in the

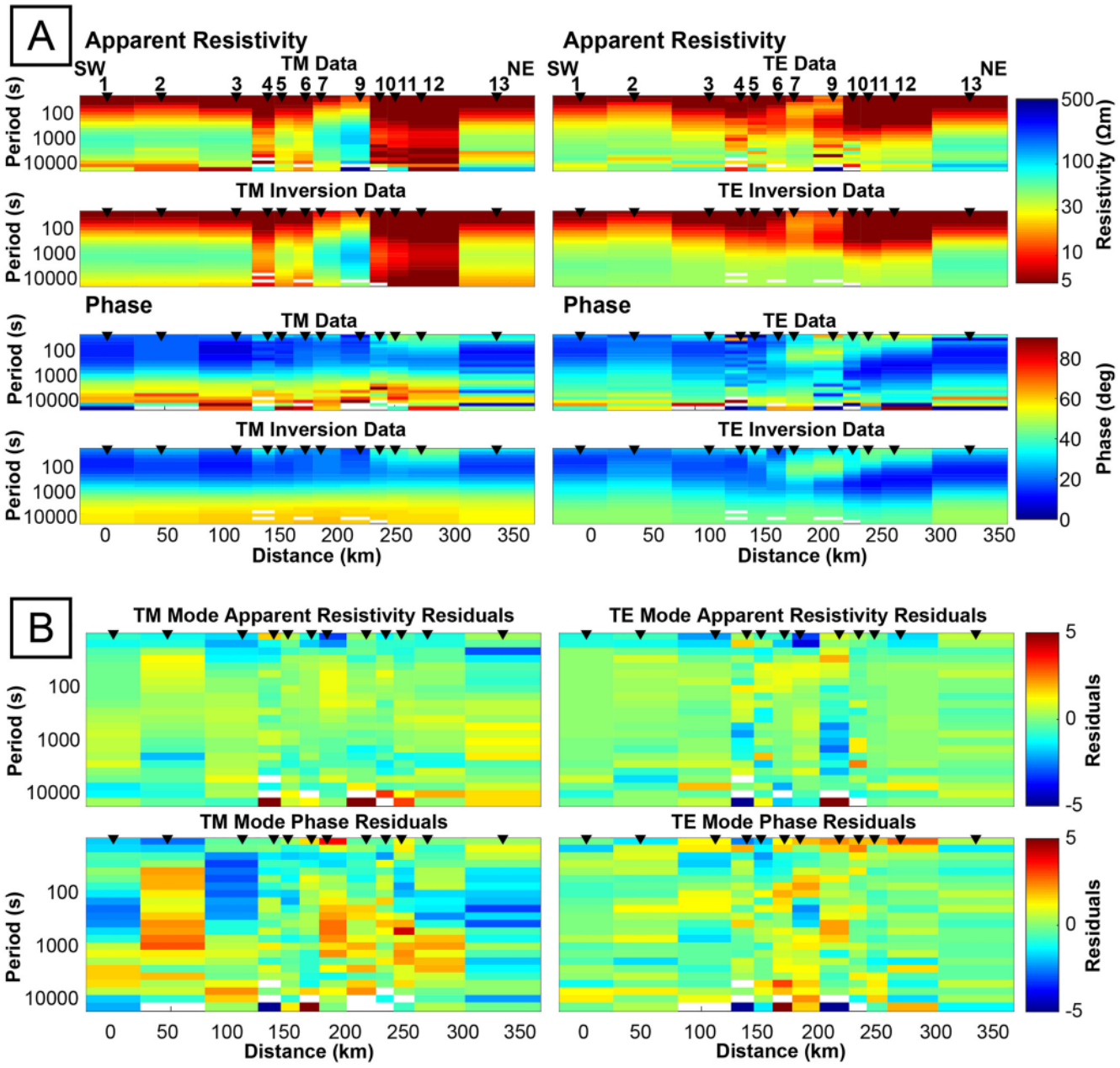

Figure 3. (a) Pseudosections comparing the apparent resistivity and phase for the transverse magnetic (TM) and transverse electric (TE) modes between the data and the inversion model in Figure 4. (b) Pseudosections of the error residuals for the apparent resistivity and phase for the TM and TE modes after inversion.

data, the inversion routine was allowed to invert for them using a 20% error floor. The tipper data was not used in the inversion as the induction vectors showed sensitivity to either the adjacent basins or features SSE of the study area. Station 8 had large static shifts and was ultimately excluded from the inversion (site with a black x in Figure 1). Given that relatively few MT sites were collected for this study, the model obtained with an inversion that included station 8 is included in Supporting Information S1 for completeness (Figure S3b in Supporting Information S1). Additional attempts to correct for the static shift at Station 8 before inverting the data involved both manually estimating the static shift and only allowing the inversion algorithm to correct for static shifts at Station 8 (Figure S3 in Supporting Information S1). Both attempts resulted in increases in RMS misfit (Figure S3 in Supporting Information S1). Further, manually estimating the static shift for Station 8 is difficult due to the nearest sites being located 20 km away, a distance over which the structure could change considerably given the area is within the SOA. The inversion used a grid with a horizontal cell size of 5 km, which provided a

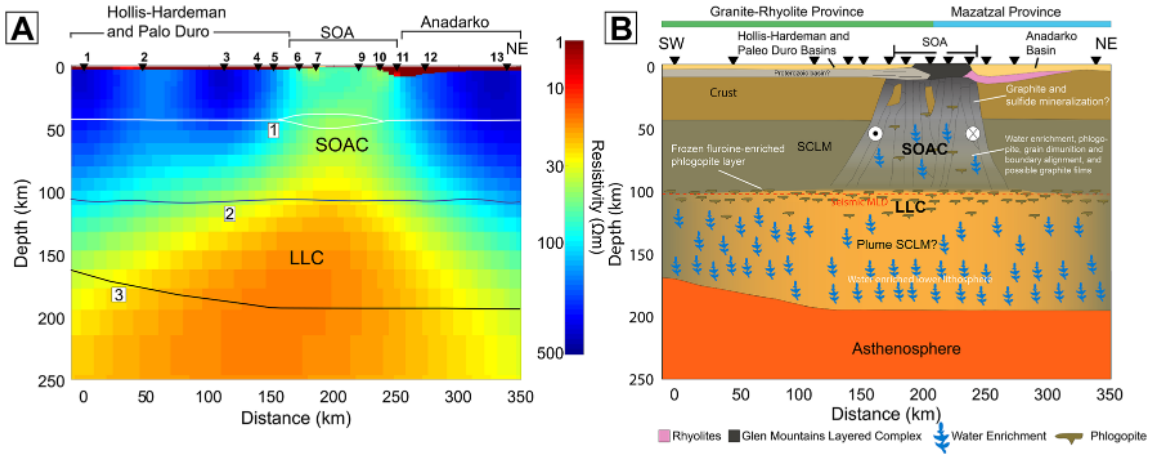

Figure 4. (a) Preferred inversion model of the remaining 12 stations. Various drawn lines are as follows. (a) Moho and rift pillow beneath the Southern Oklahoma Aulacogen (SOA) (Tave, 2013); (b) mid-lithosphere discontinuity (MLD) (Kumar et al., 2012); and (c) Lithosphere-Asthenosphere Boundary (Yuan & Romanowicz, 2010). (b) Schematic summary cross section of interpretations for the SOA beneath the profile. The analysis leading up to this model will be done in Section 4. Blue shapes represent hydrogen enrichment, green-brown shapes represent the frozen melt phlogopite-MLD layer. Seismic MLD from Kumar et al. (2012). Proterozoic basin is from Brewer et al. (1983) and Pratt et al. (1992). Sense of strike-slip movement during Ancestral Rocky Mountain deformation is from Chase et al. (2022). Note that the boundary between the Granite-Rhyolite and Mazatzal province is speculative and should not be taken as a definitive marker.

suitable tradeoff between computation time and imaging of interstation resistivity features. In the vertical direction, the first layer had a spacing of 500 m and the thickness of rows increased geometrically downward with a factor of 1.1. The inversion algorithm seeks the smoothest resistivity model that fits the measured MT data within a specific tolerance, and a range of models can be found depending on the degree of smoothing applied. The degree of spatial smoothing can be varied with the trade-off parameter τ. A range of inversions were undertaken using values of τ ranging from 0.01 to 300. The RMS misfit and roughness results are plotted as an L-curve in Figure S4 in Supporting Information S1, and the smoothing factor was set to 10 based on L-curve search criteria.

An initial inversion started from a model that was a 100 Ωm half-space. The RMS misfit started at 3.75 and the inversion converged to an RMS misfit of 1.49 after 96 iterations. The data fit is illustrated in Figures S5 and S6 in Supporting Information S1, and shows a good fit to the measured data, but a general overestimation of apparent resistivity values at short periods. The resulting model (Figure S7a in Supporting Information S1) shows a low resistivity surface layer that can be identified as the sedimentary basins. However, they extend to unrealistic depths in excess of 10–20 km, which is greater than the known sedimentary basin structure and depths (Perry, 1989). This is due to the smoothing imposed by the 2-D inversion on the resistivity model. This problem can be overcome by using knowledge of basin depth to impose constraints on the inversion. A second inversion allowed the resistivity model to have a discontinuity at the base of the sedimentary basin where the requirement for resistivity model smoothness was not imposed that is, a tear. Smoothness was imposed on the remainder of the resistivity model. This starting model incorporated the sedimentary basin as a 4 Ωm layer with a 100 Ωm basement layer below. The resistivity of both layers was permitted to vary as the inversion proceeded (Figure S7b in Supporting Information S1). The basin depths were taken from seismic, drilling and isopach data from Laske et al. (2013), Perry (1989), Davis et al. (1988), and Brewer et al. (1983). The resulting inversion model is shown in Figure 4. It started with an RMS misfit of 3.75 which was reduced to 1.19 after 102 iterations. The fit between the measured MT data and inversion model response is shown in Figure 3 and Figure S8 in Supporting Information S1. Comparison of the residual errors in pseudosection format in Figure 3b and Figure S8b in Supporting Information S1 shows that allowing the tear gives a better fit particularly in the shorter periods. A reference model was not used in the inversion, and the sensitivity of the model was instead evaluated using the process outlined in Section 3.4.

The final model (Figure 4) contains the following resistivity features:

- A 1–10 Ωm conductor extending from the surface to a depth of 3–12 km, corresponding to the Holis-Hardeman and Anadarko sedimentary basins, respectively. This low resistivity is due to the presence of sedimentary rocks and associated pore fluids found in these basins.

- An underlying 200–400 Ωm resistive layer stretching over most of the study area in the depth range 5–100 km. Given the relative insensitivity of MT to high resistivity regions, and possible downward smoothing of overlying conductors, the resistivity values of this layer may be underestimated.
- An interruption of this resistive region below the SOA is observed where resistivity values decrease to 40–60 Ω-m. This feature is referred to as the SOA Conductor (SOAC).
- Below a depth of 100 km, the resistivity again decreases to 20–30 Ω-m over a broad region, which continues through the bottom of the model and is referred to as the Lower Lithosphere Conductor (LLC).

Both conductors (SOAC and LLC) are significant because they have resistivity values much lower than the high values (100–10,000 Ωm) typically observed in basement rocks found within the crust and mantle of stable lithosphere (Selway, 2014).

3.4. Sensitivity Analysis

To evaluate the sensitivity of the measured MT data to the features present in the preferred model, a variety of tests were performed. This included both synthetic inversions and forward modeling.

A synthetic inversion approach was investigated and is illustrated in Supporting Information S1. A model was developed with a low resistivity feature to represent the LLC (Figure S9a in Supporting Information S1), SOAC (Figure S9b in Supporting Information S1), and the more resistive basement region (Figure S9c in Supporting Information S1). Resistivity values were selected so that they matched those observed in Figure 4a. The LLC was modeled as a 20 Ω-m main block that extended to a depth of 300 km with a 50 Ω-m layer above. Both features extended flat to the edge of the space. A forward calculation was used to generate synthetic MT data, and noise at 5% was then added. These data were then inverted using the same approach as for the field data. The synthetic inversion model obtained showed that this layer could be imaged (Figure S9a in Supporting Information S1). It also showed that the resistivity of this layer was lowest beneath the center of the profile. The true model had a flat geometry, but the inversion produced a model where the layer deepens at the ends of the profile (Figure S9a in Supporting Information S1). The SOAC was represented as a 50 Ω-m block, and the synthetic inversion model shows that this feature can be imaged within the surrounding 100 Ω-m half-space (Figure S9b in Supporting Information S1). Finally, the resistive basement was included as a 275 Ω-m halfspace. This value was chosen as a median value of this layer below MT sites located away from the SOAC. Including the resistive feature further centralizes the lowest resistivity values in the LLC beneath the center of the profile (Figure S9c in Supporting Information S1). It also has the effect of making the deepening of the LLC on the flanks of the profile more pronounced. A further test evaluated how the model in Figure S9c in Supporting Information S1 varied with the amount of added noise and error floors applied to the inversion. To simulate the measured MT data, 20% and 5% noise were added to the apparent resistivity and phase, respectively. The error floors in the inversion were assigned similar values and the resulting inversion model is shown in Figure S9d in Supporting Information S1, and here the SOAC anomaly is not recovered by the inversion. This suggests that the 20% noise added to the apparent resistivity is greater than the subtle response of the SOAC anomaly. This suggests that a noise level of 20% was likely an overestimation of the noise level in the measured MT data at period ranges sensitive to the SOAC anomaly. Additional tests not included in this paper showed that the extent of this deepening on either side of the SOA were heavily influenced by the depth extent and geometry of the tear region used to model the Anadarko and Holis-Hardeman basins.

To evaluate if the SOAC and LLC are robust and required by the MT data, the preferred inversion model in Figure 4a was modified to remove these resistivity features. This modified model was then used as the starting model for a new inversion. This was done as follows:

- The SOAC was modified by replacing it with a 275 Ω-m resistivity. A forward calculation was performed for this model, and it was found that the editing increased the RMS misfit from 1.19 to 2.426. The inversion was then allowed to run, and it converged to 1.262 after 88 iterations which was close to the original misfit (Figures S10 and S12 in Supporting Information S1).
- The LLC was modified by replacing it with a 100 Ω-m resistive feature in the depth range from 100 to 300 km. A forward calculation was performed, and it was found that editing the model increased the RMS misfit from 1.19 to 2.587. The inversion converged to an RMS misfit of 1.440 after 112 iterations (Figures S11 and S12 in Supporting Information S1).

The significant increase in RMS misfit for both the edited models shows that the SOAC and LLC are well resolved by the measured MT data.

4. Resistivity Model Interpretation

Zones of low resistivity have been frequently reported in regions of stable lithosphere globally (Aulbach, 2018; Selway, 2014, 2018). These anomalies may be due to several factors that include elevated temperature conditions, lithosphere grain boundary alignments alongside grainsize reduction, enrichment of nominally anhydrous minerals (NAMs) in water as OH^- ions dissolved in the mineral lattice, and the presence of fluids, melts, exotic minerals such as sulphides and graphite, or hydrous minerals such as phlogopite and amphibole. It is important to determine the cause of these low resistivity anomalies because they can address important questions about tectonic assembly, lithospheric evolution and survival, and mineral exploration. This section will explore the causes of the low resistivity features observed in Figure 4a in relation to the mechanisms listed above. The interpretations will build into the final schematic summary presented in Figure 4b.

4.1. Temperature, Fluid, and Melt Conditions

The temperature at depth is a key parameter controlling mantle resistivity and can determine if certain conduction mechanisms can occur. A geotherm was constructed using the surface heat flow and temperature estimates from xenoliths. A key challenge in this task is that heat flow represents present day conditions, while xenoliths represent temperature conditions in the past. Garnet xenocrysts from kimberlite pipes with an age of 106 Ma in nearby Arkansas support a relatively cool geotherm, consistent with a heat flow of 35–40 mW/m^2 (Griffin et al., 2004, 2011). This region of Arkansas has experienced the same tectonic history as the SOA making the Arkansas geotherm a useful analog, and available xenocrysts postdate the major heat-producing tectonic episodes. While earlier rifting or orogenesis could have perturbed and increased temperatures, the rifting occurred too far into the past for perturbations to remain today (Kaminski & Jaupart, 2000). Further, the temperature effects of orogenesis would have rapidly re-equilibrated due to the narrowness (~100 km) of the SOA (Gaudemer et al., 1988). As a result, we use the geotherm consistent with a heat flow of 40 mW/m^2 from Hasterok and Chapman (2011) for modeling. Other geotherm estimates in the region are derived from boreholes drilled into the sedimentary basins and may overestimate the subsurface temperatures as a result of the lower thermal conductivity of the sedimentary units (Blackwell et al., 2006). Figures 5a and 6a show temperatures that are far below the dry peridotite solidus with this geotherm. Sections 4.2.1 and 4.3.2 below examine the possibility of peridotite being enriched in water content due to tectonism. This enrichment would lower the peridotite solidus curve, potentially resulting in melt generation. However, this melt would have to somehow survive past the post-tectonic thermal re-equilibration previously mentioned and well as remain in the lithosphere far longer than estimated residence times (McKenzie, 1985). Further, if melt were present, we would expect seismic velocity reductions far greater than those observed beneath the SOA today (Evanzia et al., 2014). Given this, it is unlikely that the anomalies present in the resistivity model (Figure 4) reflect relict high temperatures related to either past tectonic episodes or the presence of partial melt. It is also unlikely that these anomalies reflect the presence of relict aqueous fluids since porosity is very low at these depths and fluids will have migrated out of the system since the cessation of tectonic activity (Selway, 2014, and references therein). Given that neither melt or aqueous fluids phases are unlikely explanation, assessing the viability of additional conductivity phases for explaining the SOAC and LLC will be done independently.

4.2. Origin of Southern Oklahoma Aulacogen Conductor (SOAC)

The MATE program of Özaydın and Selway (2020) integrates decades of mantle mineral physics experiments in order to interpret MT data and was used here to determine which conductivity phases could explain the 40–60 Ω-m resistivity of the SOAC anomaly. Given the lack of xenolith constraints for the composition of the SOA SCLM, the generic composition model for Proterozoic aged lithosphere of Griffin et al. (2004, 2011) was used. MATE also requires estimates of additional parameters such as mineral solubility limits, water partitioning, Al_2O_3 content in orthopyroxene, and mineral conductivity models. Most parameter choices have a minimal impact on conductivity results, and the choices for these parameters and justifications are provided in Supporting Information S1. The final bulk resistivity value for each model produced by MATE was calculated using the multi-phase Archie's Law of Glover (2010).

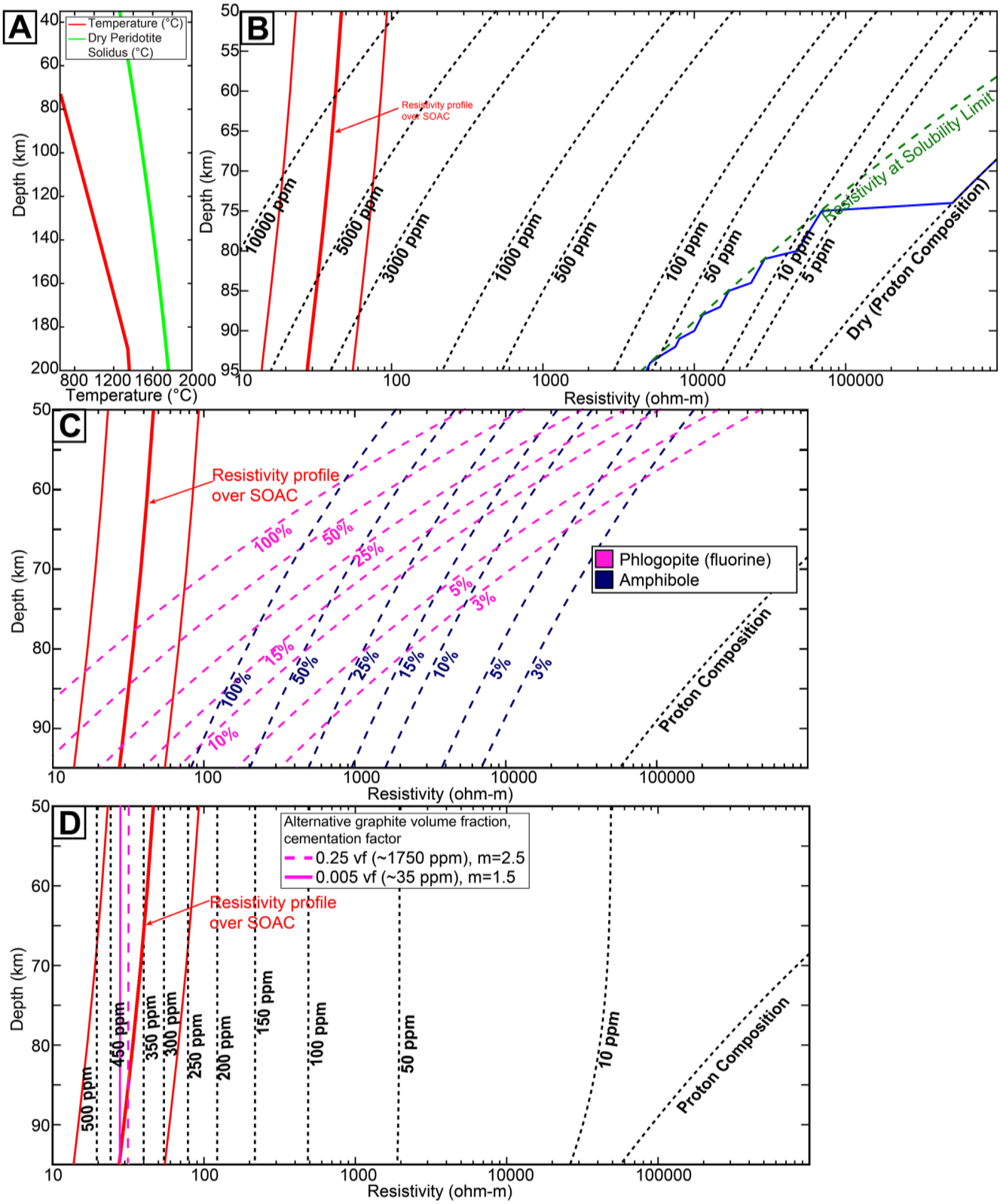

Figure 5.

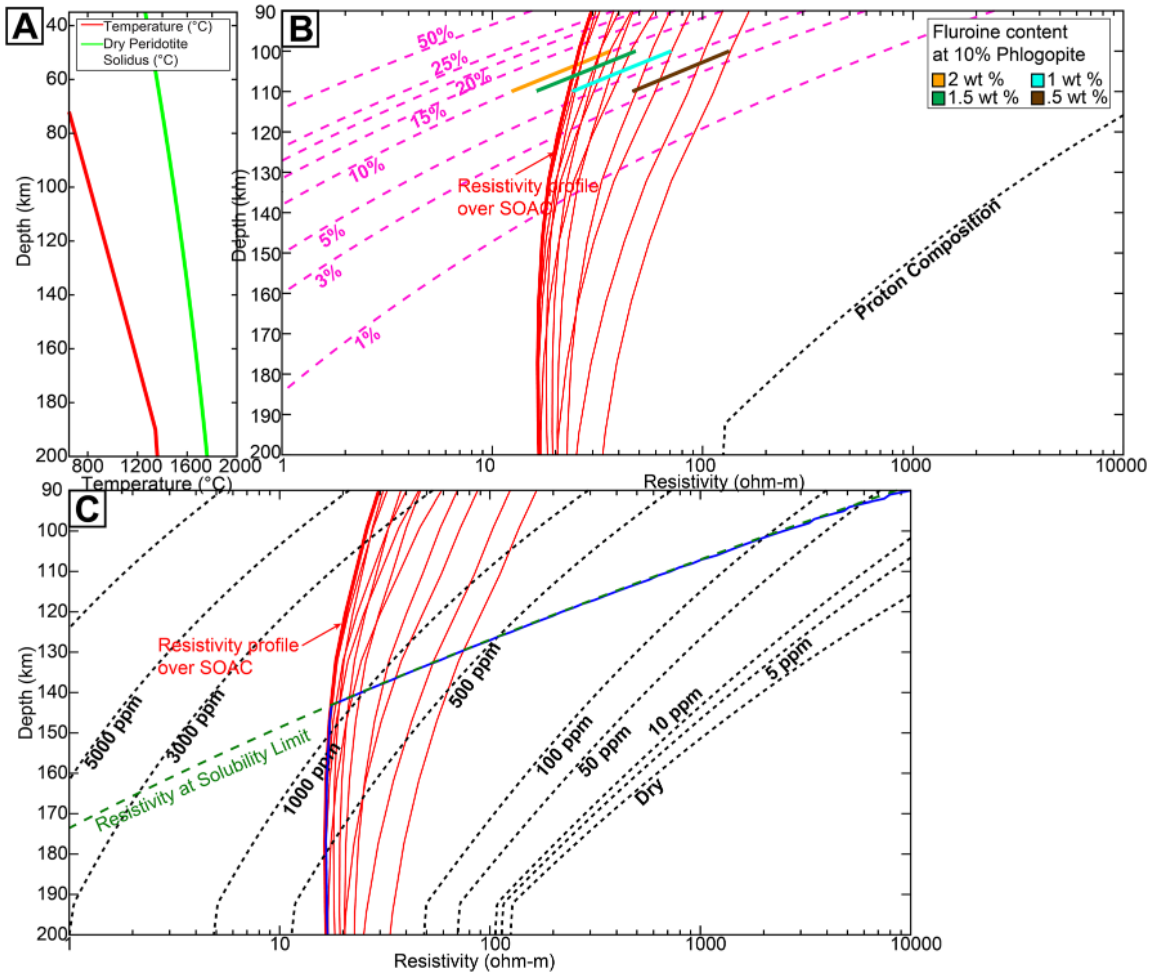

Figure 6. (a) The same geotherm from Figure 5a. (b, c) Results of MATE analysis for the Lower Lithosphere Conductor and the lines are structured the same as Figure 5. (b) Resistivity as a function of different percentages of the matrix being made up of phlogopite with 2 wt % fluorine. The various color-coded lines are the resistivity profiles for a fluorine enriched phlogopite-mid-lithosphere discontinuity with different wt % of fluorine. The yellow box denotes the combined minimum-maximum resistivity values that are 1 standard deviation from these main profiles. (c) Resistivity as a function of different ppm bulk water content. The blue line is the resistivity profile that can be made though only water incorporation in peridotite while respecting the solubility limit. It shows that for a site central to the Southern Oklahoma Aulacogen water incorporation can explain the resistivity anomaly at depths >150 km.

4.2.1. Water Enrichment in Nominally Anhydrous Minerals (NAMs)

The enrichment of nominally anhydrous mantle minerals (NAMs) with water has been proposed as an explanation for low resistivity in the depth range from the mid-crust to the base of the lithosphere (see Selway (2014), and references therein). Since olivine is the dominant, most interconnected mineral phase in the SCLM it exerts a primary control on the bulk resistivity. As a result, MATE parameters related to its solubility limit and enrichment conductivity model are among the most important to define. Here, the olivine conductivity model of Gardés et al. (2014) was used as it incorporates the errors and uncertainties of previous laboratory studies. The solubility limit of Padrón-Navarta and Hermann (2017) was used as it avoids super solidus temperatures, supercritical fluid phase condition issues, and used a multi-grained natural peridotite.

Figure 5. (a) Red line, 40 mW/m^2 geotherm from Hasterok and Chapman (2011) used for the region; green line, Dry Peridotite Solidus from Hirschmann et al. (2009). Note that the temperature does not cross the solidus, suggesting melt is not found in the region. (b–d) Results of MATE analysis for the Southern Oklahoma Aulacogen Conductor (SOAC). The thick red line in each image is the resistivity profile central to the SOAC station. The outer thinner red lines are the resistivity values within the error range of the data. (b) Analysis of resistivity as a function of different ppm bulk water content in peridotite (black dashed lines). The green line is resistivity at the solubility limit for peridotite from Padrón-Navarta and Hermann (2017). Note that black lines left of the green line are over the storage capacities of the minerals. (c) Resistivity as a function of different percentages of the matrix being made up of amphibole (blue) or phlogopite with 2 wt % fluorine (pink). (d) Resistivity as a function of moderately well connected ($m = 2$) ppm graphite in the matrix (black dashed lines). The pink lines are calculations of resistivity as a function of graphite content with different cementation factors and ppm.

Figure 5a displays the variation of bulk resistivity as a function of water content in NAMs using MATE. It shows that the observed resistivity of 40–60 Ω-m would require a concentration of 3,000–10,000 ppm of bulk water (i.e., total water content in clinopyroxene, orthopyroxene, garnet, and olivine), or 600–1,300 ppm in olivine, decreasing with depth. This far exceeds the saturation limit of NAMs at these depths (Padrón-Navarta & Hermann, 2017), which range from 0 to 100 ppm of bulk water, with 0–30 ppm in olivine (Figure 5b). To explain the resistivity of the SOAC anomaly in terms of water enrichment would require a combination of water in the NAMS in addition to some free fluids. As mentioned above, the significant time since tectonism makes it is unlikely that free fluid phases are still present.

While water enrichment in NAMs is not capable of explaining the entire anomaly of the SOAC it may still partially contribute to it, particularly in lithosphere mantle regions. The viability of water as a conductivity enhancing mechanism in the context of the tectonic history of the SOA then deserves consideration. Water enrichment occurs when tectonothermal events such as rifting introduce metasomatic fluid fluxes into the lithosphere (Bell & Rossman, 1992; Hofmann, 1997; Martin, 2006). Since water is incompatible during partial melting (Arth, 1976; Aubaud et al., 2004; Salters et al., 2002), to avoid depletion requires either limited partial melting or enrichment during the final stages of tectonism. At all stages of SOA rifting the genesis of magmatic products appears to have produced limited or no partial melting of the lithosphere (Brueseke et al., 2016; Hanson et al., 2013; Lidiak et al., 2014; Price, 2014; Wall et al., 2021), allowing any enrichment to escape subsequent depletion. The abundant A-type felsic and tholeiitic subalkaline mafic units in the SOA argue that the water content of magmas were 2–5 wt % (Bonin, 2007; Brueseke et al., 2016; Clemens et al., 1986; Dall-Agnol et al., 1999; Forst & Lindsley, 1992; Hanson et al., 2013; Hogan & Gilbert, 1995; Klimm et al., 2003; Martin, 2006).

While the low resistivity of the SOAC anomaly cannot be explained by water enrichment alone, the chemistry and evolution of the SOA during rifting argues that water content likely contributes to the lower resistivity values.

4.2.2. Hydrous Minerals

Metasomatic processes in the lithosphere often produce hydrous mineral phases such as phlogopite and amphibole (O'Reilly and Griffin, 2013). These minerals often have lower resistivity values than surrounding mantle peridotite (Selway, 2014, 2018). Both amphibole and phlogopite are often deposited as veins or dikes (S. Foley, 1992; S. F. Foley & Fischer, 2017) which means that they are likely to form well-connected systems in the mantle and can have a large effect on bulk resistivity at small volumes. The conductivity of phlogopite can be further enhanced through enrichment in the primary charge carrier fluorine (Li et al., 2016, 2017). In the SOA, fluorine could have been supplied by the same phases that ultimately produced the fluorine-rich A-type magmatism during rifting (Bonin, 2007; Hanson et al., 2013; Hogan & Gilbert, 1995; Martin, 2006; Price et al., 1999).

The effect of phlogopite on resistivity was modeled in MATE and is shown in Figure 5c. We modeled both amphibole and phlogopite with cementation factors of $m = 1.3$, reflecting a well-connected system. No xenolith data were available to constrain the fluorine content, so a value of 2 wt % was used. No xenolith data were available to constrain the fluorine content, so a value of 2 wt % were used. The upper value is an approximate average value for phlogopite xenoliths collected by Li et al. (2016). The results in Figure 5c show that phlogopite concentrations in the range 10%–50% can explain the bulk resistivity of the SOAC.

Phlogopite is often produced by metasomatic processes associated with alkaline fluids (Grégoire et al., 2002; O'Reilly & Griffin, 2013; Safonov et al., 2019). These fluid species are associated with the genesis of A-type felsic rock (Martin, 2006) common to the SOA (Brueseke et al., 2016; Hanson et al., 2013). Hydrous minerals are also seismically slower than surrounding lithosphere, and so seismic data can be used to confirm their presence. The minimum concentration of phlogopite required by the resistivity is 10% and would produce a corresponding ∼4% reduction in seismic shear wave velocities (Rader et al., 2015). The larger amounts of amphibole necessary would produce considerably higher seismic anomalies. At 75 km beneath the SOA a reduction in shear wave velocities on the order of 2%–4% has been reported (Evanzia et al., 2014), requiring a 5%–10% concentration of phlogopite (Rader et al., 2015). These values are generally below the percentages necessary to produce the observed resistivity of the SOAC (Figure 5c). As a result, while phlogopite is not capable of explaining the observed resistivity values alone, it may contribute to both the resistivity and seismic anomalies, and its presence is possible based on the tectonic history.

Amphibole cannot explain the bulk resistivity of the SOAC, even if the rock was composed of pure amphibole (Figure 5c). However, it has been proposed that amphibole is also a main carrier of fluorine in the mantle (Aiuppa

et al., 2009; Smith, 1981). This could enhance the conductivity of amphibole by a similar mechanism to that which occurs in phlogopite (Li et al., 2017). Evidence from xenolith data shows that amphibole occurrences are widespread at pressures <3 GPa (~100 km) (Selway et al., 2015 and references therein) making it a viable conduction mechanism in the upper lithospheric mantle. However, the mineral physics experiments critical in evaluating the fluorine and amphibole conductivity relationship have not yet been performed. This data is needed in order to accurately evaluate the role of amphibole in producing low resistivity anomalies in the mantle.

4.2.3. Graphite

Graphite films are stable in the lithosphere and are often invoked to explain low resistivity features. Experiments show that if the films are thick enough, they will be interconnected up to a temperature of 1000°C (~130 km beneath the SOA) (Yoshino & Noritake, 2011; Zhang & Yoshino, 2017). However, xenoliths have only shown graphite film stability to ~600–900°C (~65–115 km) (Mathez, 1987; Mathez et al., 1984; Pineau & Mathez, 1990). Additionally, even at lower temperatures graphite film stability may be transient feature, becoming disconnected over just a few tens of thousands of years (Yoshino & Noritake, 2011). With this background, the MATE software was used to investigate if the bulk conductivity of the SOAC could be explained by graphite films. The results show that with a cementation factor of $m = 2$, graphite concentrations of 300–500 ppm can produce the observed resistivity of the SOAC (Figure 5d). The amount of graphite required is highly sensitive to the cementation factor. For example, producing SOAC resistivity values can require as much as 1,750 ppm when $m = 2.5$ or as little as 35 ppm if $m = 1.5$ (Figure 5d).

What would be the source of the carbon? The enriched OIB source for SOA rift magmatism can have carbon concentration for 50–500 ppm (Dasgupta & Hirschmann, 2010), meeting the ~100 ppm concentrations necessary for lowering mantle resistivity (Duba & Shankland, 1982). The reducing conditions responsible for SOA tholeiitic magmatism also promote graphite stability (Forst & Lindsley, 1992; Stagno & Frost, 2010). Graphite formation and deposition could have been accomplished by a reduction of a CO_2 fluid phase common for rift zones (Brune et al., 2017; S. F. Foley & Fischer, 2017) and in the genesis of A-type granitic magmas (Martin, 2006). However, the nephelinitic and carbonatitic volcanic units associated with this phase (Martin, 2006) have not been reported in the SOA. Further, chemical reduction of CO_2 appears incapable of wetting silicate grain boundaries, producing graphite that would be isolated and poorly conducting (Watson & Brenan, 1987; Yoshino & Noritake, 2011; Zhang & Yoshino, 2017). Oxidation of CH_4-rich fluid species could also result in the formation of graphite films (Stachel & Luth, 2015), but the SOA magmatic units leave the role of this fluid species unclear and argue for reducing conditions. As a result, the viability and stability of graphite films produced by fluids in a rifting environment appears unlikely for the part of the SOAC located in the SCLM. Previous authors have argued this conduction mechanism system could be stable in the crust (e.g., Murphy et al., 2022), but few laboratory observations have been made for this type of system.

Another factor relevant to the discussion of graphite is the secondary deformation and shearing that occurred during the later-stage ARM (Chase et al., 2022; Granath, 1989). This could have potentially mobilized, smeared, and interconnected previously deposited and isolated graphite (Glover & Ádám, 2008; Puelles et al., 2014). This is similar to interpretations of graphite-related low-resistivity anomalies in both orogenic and shear zones systems (e.g., DeLucia et al., 2019; A. G. Jones et al., 2005). The caveat to this interpretation is that grain boundary films could still become disconnected over time, as observed in typical mantle olivine aggregates (e.g., Zhang & Yoshino, 2017). However, if interconnection was accomplished along zones of structure weakness like those created during rifting, these can be longstanding features that are resistant to healing (Bercovici & Ricard, 2012), which may provide for long-term graphite film stability.

Despite the difficulty to initially establish grain boundary graphite films, the tectonic, and magmatic history of the SOA appears favorable for both introducing graphite and establishing interconnection sufficient to produce the resistivity values observed in the SOAC. However, the volcanic history of the SOA does not suggest the prominence of carbon-bearing fluids or the conditions necessary to form graphite. Additionally, the long-term stability of these films appears tenuous (Yoshino & Noritake, 2011). Given that it is a prominent phase to explain low resistivity anomalies elsewhere we do not rule it out, but suggest it is unlikely to explain the SOAC.

4.2.4. Sulfide Minerals

Sulfides minerals are another viable candidate to explain low resistivity and are stable throughout the mantle lithosphere (Selway, 2018). Sulfides have conductivity values similar to graphite (Saxena et al., 2021), and resistivity

calculations give results similar to those for graphite. Prior studies have suggested that large igneous provinces such as the SOA can host significant amounts of sulfide minerals (M. J. Jones et al., 2016), and layered complexes such as the Glen Mountain Layered Complex of the SOA can host large quantities of sulfides phases (Godel et al., 2006; Zientek, 2012). However, occurrences of sulfides in drill core from the SOA are few, and largely limited to the diabase dikes (Brueseke et al., 2016; Ham et al., 1964; Hanson et al., 2013; Lidiak et al., 2014; Puckett et al., 2014). The sulfide concentrations necessary to significantly reduce resistivity are high, >6 vol.% (Saxena et al., 2021), and at these concentrations we would expect to see the presence of sulfides noted far more often in geologic studies of SOA rock units. Given these constraints, it is unlikely the low resistivity of the entire SOAC can be explained by the presence of sulfides minerals. However, if present, sulfides may be a plausible mechanism in the shallow to mid crust, particularly along volcanic conduits.

It should be noted that this study uses long-period MT data, which has generally poor sensitivity to the upper crust. As a result, resistivity values in the upper crustal portion of the SOAC are likely to be poorly constrained.

4.2.5. Grain Size Reduction

The conductivity of olivine in the upper mantle can be enhanced by a reduction of average grain size and the alignment of grain boundaries, which provide better pathways and more surface area per unit volume for conduction (Pommier et al., 2018; Ten Grotenhuis et al., 2004). With increasing shear strain from 1.3 to 7.3 and temperatures from 800 to 1200°C, resistivity values of olivine can range from 1,000 to 10 Ωm (Pommier et al., 2018).

Given the pronounced vertical uplift, crustal shortening and strike-slip deformation that occurred along the SOA during the ARM, a corresponding reduction in the olivine grain size is plausible. However, post-tectonic annealing would have increased the grain size and lowered the conductivity over time (Pommier et al., 2018). However, in a polycrystalline lithosphere assemblage, this process is suggested to have a timescale of hundreds of millions of years (Bercovici & Ricard, 2012). Deformation in the SOA occurred ∼300 million years ago, which supports the idea that deformation effects could persist to the present day.

Strain related to the ARM is estimated to be approximately 3.6 from the analysis of sedimentary basins located near the SOA (Craddock et al., 1993). If these estimates are also representative of the conditions experienced by the SOA lithosphere, this could produce resistivity anomalies in the range 900–1,100 Ωm in the SOAC SCLM (Pommier et al., 2018). These resistivity values are far higher than those observed in the SOAC. As a result, while grain size reduction and boundary alignment cannot explain the SOAC alone, based on the tectonic history it could still contribute to the observed resistivity anomaly.

4.2.6. Summary of SOAC Conductivity Mechanisms

Given the tectonic and magmatic history of the SOA it is proposed that the low resistivity of the SOAC is due to a combination of mechanisms that includes the presence of hydrous minerals such as (a) phlogopite, (b) elevated water content in NAMs, and (c) a reduction of olivine grain size. Graphite and sulfide films are also capable of explaining the low resistivity of the anomaly, but are unlikely candidates given the reasons above.

However, in the crust at depths less than 30 km, many of the mechanisms listed above will have minimal impact on resistivity values with the exception of graphite and sulfides. While we discount these conductive phases due to their paucity in regional geologic data, we acknowledge that the low resistivity of the crustal portion of the SOAC is likely to be better explained by them. Additional study of the shallow subsurface in the SOA would be useful in evaluating these mechanisms.

4.3. Origin of Lower Lithosphere Conductor (LLC)

The LLC begins at a depth of around 100 km as a 20–30 Ω-m horizontal layer that extends laterally and downward over the profile. At 100 km depth temperatures exceed 800°C (Figure 6a) and pressures are greater than 3 GPa. Under these mantle conditions graphite films cannot explain the low resistivity of the LLC anomaly due to film instability over geologic timescales (Yoshino & Noritake, 2011; Zhang & Yoshino, 2017). Similarly, sulfides cannot explain the LLC anomaly as they are unlikely to be present over such a large area (Selway, 2018). The remaining phases viable to explain the low resistivity of the LLC are either hydrous mineral phases such as phlogopite (Li et al., 2016, 2017), or enrichment of NAMs in water. The viability of each of these mechanisms is examined below.

4.3.1. Hydrous Mineral Phases

Due to its stability in the lower lithosphere, phlogopite is the hydrous mineral most likely responsible for the low resistivity of the LLC (Frost, 2006; Safonov et al., 2019). Extending the modeling of phlogopite from Section 4.2.2 shows that a phlogopite concentration in the range 1%–15%, and which decreases with depth, could produce the resistivity values observed (Figure 6b). These would produce a corresponding reduction in seismic velocity in the range from 0.5% to 7% (Rader et al., 2015). Coincident with the start of the LLC at 100 km, a MLD is observed in receiver function data as a 5%–7% reduction in shear wave velocities (Kumar et al., 2012). More regionally, seismic tomography data show a 2%–4% reduction in shear wave velocities in the lower lithosphere beneath the SOA (Evanzia et al., 2014).

Explanations for MLDs at this depth suggest they may form as a result of metasomatic fluids/melts becoming frozen and crystallizing phlogopite upon encountering an increase in the solidus of peridotite found at depths less than 80–100 km, perhaps reflecting a paleo LAB (Hansen et al., 2015; Rader et al., 2015; Selway, 2018). Notably, phlogopite rich xenoliths are also often extracted from this depth (Aulbach, 2018; and references therein). The MATE software was used to model an MLD as a 10 km thick layer from 100 to 110 km with 10% phlogopite, in line with MLD thickness estimates by Rychert et al. (2010), and to match the observed seismic velocity reductions (Rader et al., 2015). As with the SOAC, a fluorine concentration of 2 wt % fluorine was used for the phlogopite. The results show that resistivity values at the top of the LLC can be fit by this layer (Figure 6b). The difference in resistivity between MT stations can be explained by varying the fluorine concentration from 0.5 to 2 wt %, which spans the range of values observed in the bulk of xenolith samples compiled by Li et al. (2016) (Figure 6b).

Amphibole, as pargasite, stability extends up to a pressure of ∼3 GPa, which corresponds to a depth of 100 km, and is coincident with the top of the LLC and MLD. This led Selway et al. (2015) to suggest that MLDs may be explained by significant amounts of amphibole that could have formed along a crystallization front at the maximum pressure stability. The authors show that 11%–25% amphibole could produce a velocity reduction >5%, similar to what is observed beneath the SOA (Figure 11 in Selway et al. (2015)). The modeling performed in Figure 5c shows that these percentages of amphibole cannot explain the resistivity values observed in the LLC. In fertile peridotite, pargasite stability can extend up to a pressure of 3.5 GPa (∼115 km) (Mandler & Grove, 2016). The amphibole concentration of 11%–25% in Figure 5c at a depth of 115 km would still produce resistivity values far higher than the LLC. As with the explanation for the resistivity of the SOAC, it is possible that fluorine will enhance the conductivity of amphibole. However, the mineral physics experiments to support this hypothesis have not yet been performed.

Below the MLD we note that the resistivity values of the LLC show limited variation. This could indicate a loss of data sensitivity due to depth and the combined effects of the overlying low resistivity layers (i.e., MLD layer and the sedimentary basins). To test this, we created a forward model that modifies the resistivity structure in Figure 4a with an MLD and a 100 Ω-m halfspace below it. The resulting inversion recovers the lower halfspace (Figure S13 in Supporting Information S1) showing the data is sensitive to the lithosphere below the MLD. As a result, the low resistivity values in this region could reflect the presence of widely disseminated phlogopite. To match the 2%–4% shear wave velocity reductions (Evanzia et al., 2014) would require 4%–8% phlogopite throughout the lithosphere. However, below 120 km this amount of phlogopite would produce resistivity values lower than observed (Figure 6b), making phlogopite a less viable explanation.

The top of the LLC that corresponds to an observed seismic MLD is well explained by a ∼10 km thick phlogopite layer that is potentially enriched in plume-derived fluorine acting as the primary charge carrier (Li et al., 2016, 2017). Amphibole offers a possible alternative interpretation (i.e., Selway et al., 2015), however, the mineral physics experiments needed to evaluate this have not yet been performed. Below 110 km phlogopite becomes a less likely explanation for the low resistivity, as the amount necessary to match observed seismic anomalies would produce resistivity values lower than observed.

4.3.2. Hydrogen in Nominally Anhydrous Minerals (NAMs)

The remaining most viable conductivity mechanism for the LLC is from the enrichment of NAMs in water. Extending the modeling in Section 4.2.2. It can be shown that a concentration of hydrogen in the range 500–3,000 ppm bulk hydrogen, 280–1,000 ppm in olivine, could produce the resistivity values observed in the LLC (Figure 6c). In the depth range 100–150 km the amount of water required is above the solubility limit of the

minerals. However, below 150 km the solubility limit is large enough that water can produce the resistivity values with 300–1,000 ppm bulk water, or 200–450 ppm in olivine, being sufficient (Figure 6c).

As with the SOAC, metasomatic enrichment of the lithosphere in water likely occurred during rifting while also escaping late-stage partial melt depletion. Additionally, this type of lithosphere keel enrichment would be in line with similar SCLM keel enrichment observed in other plume impacted regions (e.g., Aulbach et al., 2017; Bedrosian, 2016; S. F. Foley, 2008; S. F. Foley & Fischer, 2017; Özaydın & Selway, 2022). Further, the compositional changes associated with keel enrichment can produce the small reductions in shear wave velocity observed in the region (Deen et al., 2006; Evanzia et al., 2014; Griffin et al., 2009). As a result, we find that hydrogen enrichment is a good candidate to explain LLC resistivity values in the lowermost lithosphere.

4.3.3. Summary of LLC Conductivity Mechanisms

Knowledge of the tectonic and magmatic history of the SOA, combined with constraints from regional seismic data, suggest that the low resistivity of the LLC is due to a combination of conduction mechanisms. The first is the presence of a phlogopite layer from in the depth range 100–110 km that is possibly enriched in fluorine and which is coincident with a seismic MLD (Kumar et al., 2012). At greater depths, it is more difficult to explain the low resistivity with phlogopite. Conduction due to water enrichment of NAMs is the preferred explanation.

5. Implications

The MT data provide a new geophysical image of the lithosphere beneath the SOA. A summary of the interpretations for the resistivity anomalies can be found in Figure 4b. The newly imaged structure allows new insights in the tectonic history of the SOA and wider Midcontinent, which are discussed below.

5.1. The SOAC and Involvement in the ARM

The ARM orogeny remains an enigmatic tectonic episode in the geological history of North Laurentia. The associated basement uplifts are discrete, widely separated, spread across a wide region of Laurentia, and are often far removed from the various plate boundaries invoked in tectonic models to explain the ARM (see Leary et al. (2017)). Conversely, basement deformation and regional metamorphism along the suggested plate boundaries themselves is limited or nonexistent, suggesting weak collisional forces along the boundaries (Keller & Stephenson, 2007; Keller et al., 1989). This suggests that beneath the uplifts the lithosphere was uniquely relatively weak and prone to deformation.

What could have caused localized zones of weakness in the continental lithosphere? The strength of the continental lithosphere is thought to decrease with increasing lithosphere enrichment introducing hydrous (i.e., water) or Ti (as titanoclinohumite) point defects in Si vacancies of olivine (Faul et al., 2016; Fei et al., 2013; O'Reilly & Griffin, 2013; Peslier et al., 2010). Ti and water enrichment accompany each other, and both follow the enrichment state of the mantle, and Ti values are often high in rock impacted by plumes (Berry et al., 2005, 2007; De Hoog et al., 2010; Padrón-Navarta & Hermann, 2017; Rehfeldt et al., 2008). Given the sensitivity of MT data to water content (e.g., Özaydın & Selway, 2022) resistivity anomalies can be used as a proxy for determining the location of associated rheological weakening.

The resistivity structure beneath the SOAC has been interpreted to reflect metasomatic enrichment of water during Cambrian rifting. As a result, the Cambrian metasomatism could have rheologically weakened the lithosphere, making the area susceptible to reactivation during the ARM. Previous research has suggested that the ARM uplifts were localized along preexisting weaknesses (e.g., Kluth & Coney, 1981; Leary et al., 2017), particularly along paleo-rifts (Marshak et al., 2003). While the xenolith data necessary to confirm this interpretation is absent, it provides a possible mechanism for SOA participation in the ARM orogeny. Further study beneath other ARM uplifts unmodified by later tectonism (e.g., the Diablo Uplift and Central Basin Platform) will be useful to investigate the regional extent of this mechanism.

5.2. The LLC and SOA Lithosphere

5.2.1. Plume Head Accretion

The LLC resistivity anomaly suggests that the lower lithosphere was metasomatically enriched below 100 km during rifting. This type of keel enrichment has been observed elsewhere and is thought to be prevalent in regions

impacted by plumes (Aulbach et al., 2017; S. F. Foley, 2008; H. Hu et al., 2018; J. Hu et al., 2018; O'Reilly & Griffin, 2013) and is often observed in MT data (e.g., Bedrosian, 2016; Bettac et al., 2023; Özaydın et al., 2022). Additionally, in nearby Arkansas to the east the region has experienced the same tectonic events as the SOA, and here the lithosphere shows strong metasomatic enrichment, with a major component related to SOA rifting (Griffin et al., 2004, 2011). However, the depths at which melts were generated to produce the olivine and quartz tholeiitic magmatic units in the SOA required a lithosphere no thicker than ∼60–80 km during rifting (D. H. Green & Ringwood, 1967). The lithosphere today is 180–200 km thick (Priestley et al., 2018), implying that it has re-thickened since the Cambrian. Thickening by lithosphere stacking or orogenic compression (Lee et al., 2011) during the ARM orogeny (Lee et al., 2011) do not seem possible due to subduction polarity dipping to the southeast and the weak collisional forces likely limited the amount of lithosphere deformation (Keller & Stephenson, 2007; Kluth & Coney, 1981). Further, progressive cooling since rifting cannot rethicken the lithosphere to these depths (Chen, 2017).

The most viable remaining mechanism for lithosphere rethickening would be accretion of the plume head to the lower lithosphere. In this model, the plume may have been localized beneath the SOA due to the presence of (a) the thin lithosphere beneath the SOA and (b) a depleted lithosphere to the east beneath Arkansas related to the Archean Sabine microcontinent (Griffin et al., 2004, 2011). This depleted layer may have shielded the Arkansas lithosphere from extensive modification, similar to plume and rift interactions occurring today beneath the Tanzanian craton (Adams et al., 2018; Nyblade & Brazier, 2002). The plume head may have been channeled into the region of thin lithosphere beneath the SOA, similar to the model proposed by Liu et al. (2021) for the rethickening of lithosphere beneath the Slave craton. However, this type of accretion typically produces depleted and dehydrated mantle residua (Lee et al., 2011; Pearson & Wittig, 2014), which would be electrically resistive. This appears to be the case beneath the plume-drive Midcontinent Rift (MCR) further north where the lithosphere is highly resistive (Bedrosian, 2016). The difference in resistivity structure may reflect the following: (a) the short duration of SOA magmatism (∼10 My) versus the MCR (∼30 My) resulting in less depletion of the plume source (Miller et al., 2013; Wall et al., 2021); (b) and the SOA plume sources being up to an order of magnitude more enriched than the MCR (Brueseke et al., 2016; Lidiak et al., 2014; Shirey et al., 1994), and by extension containing more water. As a result, the difference in the resistivity structure could reflect the accretion of more enriched, less dehydrated plume residual material beneath the SOA compared to the MCR. A more enriched plume composition alongside seismically slow hydrous mineral phases could also explain the 2%–4% seismic velocity reduction beneath the SOA (Deen et al., 2006; Rader et al., 2015).

5.2.2. A Shallow Asthenosphere

An alterative model to plume accretion is that the regional lithosphere has remained thin (<150 km) since rifting and that the LLC represents an asthenosphere that has shallowed to a depth of 80–100 km beneath the SOA. To explain the low resistivity of the LLC observed in this study would require a damp asthenosphere containing up to a few hundred ppm of water (Naif, 2018). Modeling of seismic data led Evanzia et al. (2014) to suggest that the slow anomaly beneath the SOA may represent a conduit of asthenosphere flow from the Rio Grande Rift under the North American craton. In this scenario, the LLC would represent the electrical resistivity expression of this conduit, with the elevated water content causing the asthenosphere to be weakened and permit mantle flow (Hirth & Kohlstedt, 1996). However, seismic studies of LAB depth have shown that the lithosphere extends to a depth of 180–200 km in this region (Priestley et al., 2018; Yuan & Romanowicz, 2010). It is possible that resolving the shallowing of the asthenosphere near the SOA in these seismic studies is difficult due a combination of the narrow width of the SOA and wide seismic station spacing (Evanzia et al., 2014). However, the top of the LLC is at a shallower depth than the seismic LAB estimates over the entire model space and the LLC has a lateral extent greater than the resolution scale of the seismic data (Figure 4a). Additionally, the forward modeling results in this study suggest that the shallowing of the LLC beneath the SOA could be an artifact of the inversion process (Figure S8 in Supporting Information S1). On this basis, the plume accretion model is the preferred mechanism to explain the low resistivity of the LLC.

5.3. Mid-Lithosphere Discontinuities

The MLD beneath the SOA appears to be spatially associated with the LLC low resistivity feature. However this type of association is not always the case for MLDs (Selway, 2018). Beneath the Great Plains further north, a MLD is located at a similar depth but is not coincident with a conductor (Kumar et al., 2012). Variations in

seismic radial anisotropy (Wirth & Long, 2014) or in the content of hydrous minerals like phlogopite (Hansen et al., 2015) have been invoked to explain the seismic anomaly associated with an MLD. Seismic anisotropy is not expected to produce substantial resistivity variations (Martí, 2014), whereas an increase in phlogopite concentration can increase conductivity. Unlike the SOA the seismic MLDs beneath the Great Plain lack a coincident conductor (Bedrosian, 2016; Yang et al., 2015). If phlogopite is an acceptable explanation for MLDs (e.g., Hansen et al., 2015) the variation in electrical responses could reflect variations in fluorine content, which is moderately incompatible in the lithosphere and is expected to be extracted and depleted during lithosphere stabilization (Joachim et al., 2017; Rader et al., 2015). In this model the MLDs of the Great Plains could reflect a fluorine depleted layer. In contrast, the SOA MLD may be re-enriched in fluorine by the fluids that ultimately produced the significant amount of fluorine-rich A-type felsic magmatism during rifting (Bonin, 2007; Hanson et al., 2013; Hogan & Gilbert, 1995; Martin, 2006; Price, 2014). Interestingly, near the plume driven MCR the MLDs of the Great Plains still lack coincident conductors. Notably, the MCR was mafic-dominated and contains little magmatism of the felsic fluorine-rich A-type affinity prevalent in the SOA (J. C. Green & Fitz, 1993; Vervoort et al., 2007; and references therein). This may reflect differences in the chemistry or evolution of the plume sources between the SOA and MCR. Here, the MCR plume may have been depleted in fluorine content, or the tectonic evolution during rifting precluded introduction of fluorine into the lithosphere in the manner found in the SOA. The depletion hypothesis would be consistent with previous interpretations of a depleted lithosphere beneath the MCR (Bedrosian, 2016).

Prior work by Selway (2018) noted the variability in the resistivity signatures of MLDs. In regions of suspected phlogopite-related MLDs, enrichment in fluorine offers a potential explanation for these variations. It would also support the view of Li et al. (2016, 2017) that fluorine content is the critical parameter controlling phlogopite resistivity.

In the plume accretion model, the MLD could represent a layer of phlogopite-bearing metasomatic melts derived from the plume that froze to the base of the thinner lithosphere during rifting. This layer was then entombed during accretion of the plume head. This would be in line with suggestions that MLD represent paleo LABs (Hansen et al., 2015; Rader et al., 2015; Selway, 2018). We note that this model would be equally applicable to an amphibole layer (e.g., Selway et al., 2015) although mineral physics experiments required to show amphibole conductivity is enhanced by fluorine content have not been performed.

6. Conclusions

The south-central US provides valuable insights into the assembly and tectonic evolution of Laurentia. The area contains a variety of largely unmodified tectonic structures that are related to the breakup of Rodinia and assembly of Pangea. This study investigated one of these, the SOA, a Cambrian plume-driven failed-rift that was structurally inverted during the Paleozoic-Pennsylvanian ARM orogeny. Long-period MT data were used to produce a 2D resistivity model that was sensitive to the entire lithosphere. Two major low resistivity features are noted. The first is the SOAC, which is located in the crust and upper mantle lithosphere. The second is the LLC, which starts at a depth of 100 km and extends into the lower mantle lithosphere. The low resistivity of the SOAC is attributed to a combination of enrichment of NAMs with water and the formation of hydrous mineral phases like phlogopite via plume-lithosphere interactions during rifting metasomatism. Additional contributions to the low resistivity likely occurred during the ARM orogeny where deformation led to olivine diminution and grain boundary alignment. This deformation may have also interconnected graphite possibly precipitated by early rift fluids, however, based on mineral physics experiments and the magmatic evolution of the SOA, the stability and presence of graphite appears tenuous. The upper part of the LLC at a depth of ∼100 km is attributed to a fluorine-enriched phlogopite layer, which is coincident with an MLD imaged by seismic data. Below this region the remainder of the low resistivity of the LLC is attributed to a lower lithosphere of water enriched NAMs.

The rifting metasomatism would have likely resulted in the introduction of both water and Ti into the mantle peridotites of the SOAC. These phases would have rheologically weakened the lithosphere beneath the SOA, which permitted it to localize deformation during the ARM orogeny. This metasomatic rheological weakening model provides a possible mechanism for explaining how ARM deformation occurred only along discrete and spread-out features in the Laurentian intraplate that were far from the causative tectonic boundary forces. Evaluation of this mechanism via numerical modeling and additional geophysical sampling of the other tectonically unmodified ARM uplifts in the southern US would be useful.

The fluorine enrichment of the phlogopite MLD beneath the SOA provides a possible mechanism for explaining the variability in the electrical responses of phlogopite-derived MLDs. The enriched lower mantle lithosphere in the region represents a lithosphere that has been rethickened since rifting during the Cambrian. This would have been most readily accomplished via accretion of the plume head to the lithosphere upon rifting failure. Due to the enriched nature of the plume source and the short duration of SOA rifting, the accreted material could have remained more enriched, and therefore more electrically conductive, than typical plume accretion residua. In this model, the phlogopite MLD may reflect a melt layer deposited along a paleo lithosphere-asthenosphere boundary that was entombed during plume accretion.

The role of sulfides and graphite in lowering resistivity and explaining the crustal extension of the SOAC does not appear favorable due to the paucity of these phases in the rock record in addition stability issues with graphite films over geologic time. However, the other lithosphere conductivity mechanisms have limited impact on resistivity values in the crust. Further evaluation is needed to explain the shallower resistivity values of the SOA.

Data Availability Statement

The magnetotelluric data set used in this study is available from the University of Alberta Education and Research Archive at https://era.library.ualberta.ca/items/3b884b44-882f-48c8-aaa0-4ad64c69a9a7. The MATE software can be accessed through https://github.com/sinanozaydin/MATE.

Acknowledgments
We thank the variety of Oklahoma landowners who so graciously allowed us to place instruments on their lands. Micah Mayle, Curtis Carter, David Beckendorff, Dr. Folarin Kolawole, and Steven Johnson are thanked for their assistance in the field. We thank Sinan Özaydın for his assistance with answering technical questions regarding the MATE program. We thank Dr. Takashi Yoshino, Dr. Richard Hanson, and Dr. William Griffin for answering questions regarding on graphite in the mantle, and in SOA geology/geochemistry, and Arkansas lithosphere, respectively. Conversations with Dr. Thomas Stachel and Dr. Graham Pearson helped to develop ideas in this paper regarding interpretation. Sinan Özaydın and an anonymous reviewer are thanked for their reviews of this manuscript.

References

Abdelsalam, M. G., Liégeois, J. P., & Stern, R. J. (2002). The saharan metacraton. *Journal of African Earth Sciences*, *34*(3–4), 119–136. https://doi.org/10.1016/S0899-5362(02)00013-1

Adams, A., Miller, J., & Accardo, N. (2018). Relationships between lithospheric structures and rifting in the east African rift system: A Rayleigh wave tomography study. *Geochemistry, Geophysics, Geosystems*, *19*(10), 3793–3810. https://doi.org/10.1029/2018GC007750

Aiuppa, A., Baker, D. R., & Webster, J. D. (2009). Halogens in volcanic systems. *Chemical Geology*, *263*(1–4), 1–18. https://doi.org/10.1016/j.chemgeo.2008.10.005

Amsden, T. W. (1982). Early and middle Paleozoic history of the Anadarko basin. *Geological Society of America Abstracts with Programs*, *14*(3), 105.

Arth, J. G. (1976). Behavior of trace elements during magmatic processes—A summary of theoretical models and their applications. *Journal of Research of the U. S. Geological Survey*, *4*(1), 41–47.

Aubaud, C., Hauri, E. H., & Hirschmann, M. M. (2004). Hydrogen partition coefficients between nominally anhydrous minerals and basaltic melts. *Geophysical Research Letters*, *31*(20), L20611. https://doi.org/10.1029/2004GL021341

Aulbach, S. (2018). Cratonic lithosphere discontinuities: Dynamics of small-volume melting, metacratonization, and a possible role for brines. *Lithospheric Discontinuities*, 177–203. https://doi.org/10.1002/9781119249740.ch10

Aulbach, S., Massuyeau, M., & Gaillard, F. (2017). Origins of cratonic mantle discontinuities: A view from petrology, geochemistry and thermodynamic models. *Lithos*, *268*, 364–382. https://doi.org/10.1016/j.lithos.2016.11.004

Bedrosian, P. A. (2016). Making it and breaking it in the Midwest: Continental assembly and rifting from modeling of EarthScope magnetotelluric data. *Precambrian Research*, *278*, 337–361. https://doi.org/10.1016/j.precamres.2016.03.009

Bell, D. R., & Rossman, G. R. (1992). Water in Earth's mantle: The role of nominally anhydrous minerals. *Science*, *255*(5050), 1391–1397. https://doi.org/10.1126/science.255.5050.1391

Bercovici, D., & Ricard, Y. (2012). Mechanisms for the generation of plate tectonics by two-phase grain-damage and pinning. *Physics of the Earth and Planetary Interiors*, *202*, 27–55. https://doi.org/10.1016/j.pepi.2012.05.003

Berry, A. J., Hermann, J., O'Neill, H. S., & Foran, G. J. (2005). Fingerprinting the water site in mantle olivine. *Geology*, *33*(11), 869–872. https://doi.org/10.1130/G21759.1

Berry, A. J., Walker, A. M., Hermann, J., O'Neill, H. S. C., Foran, G. J., & Gale, J. D. (2007). Titanium substitution mechanisms in forsterite. *Chemical Geology*, *242*(1–2), 176–186. https://doi.org/10.1016/j.chemgeo.2007.03.010

Bettac, S. P., Unsworth, M. J., Pearson, D. G., & Craven, J. (2023). New constraints on the structure and composition of the lithospheric mantle beneath the Slave craton, NW Canada from 3-D magnetotelluric data–Origin of the Central Slave Mantle Conductor and possible evidence for lithospheric scale fluid flow. *Tectonophysics*, *851*, 229760. https://doi.org/10.1016/j.tecto.2023.229760

Blackwell, D. D., Negraru, P. T., & Richards, M. C. (2006). Assessment of the enhanced geothermal system resource base of the United States. *Natural Resources Research*, *15*(4), 283–308. https://doi.org/10.1007/s11053-007-9028-7

Bonin, B. (2007). A-Type granites and related rocks: Evolution of a concept, problems and prospects. *Lithos*, *97*(1–2), 1–29. https://doi.org/10.1016/j.lithos.2006.12.007

Booker, J. R. (2014). The magnetotelluric phase tensor: A critical review. *Surveys in Geophysics*, *35*(1), 7–40. https://doi.org/10.1007/s10712-013-9234-2

Brewer, J. A., Good, R., Oliver, J. E., Brown, L. D., & Kaufman, S. (1983). COCORP profiling across the southern Oklahoma aulacogen: Overthrusting of the Wichita Mountains and compression within the Anadarko Basin. *Geology*, *11*(2), 109–114. https://doi.org/10.1130/0091-7613(1983)11<109:CPATSO>2.0.CO;2

Brueseke, M. E., Hobbs, J. M., Bulen, C. L., Mertzman, S. A., Puckett, R. E., Walker, J. D., & Feldman, J. (2016). Cambrian intermediate-mafic magmatism along the Laurentian margin: Evidence for flood basalt volcanism from well cuttings in the Southern Oklahoma aulacogen (USA). *Lithos*, *260*, 164–177. https://doi.org/10.1016/j.lithos.2016.05.016

Brune, S., Williams, S. E., & Mueller, R. D. (2017). Potential links between continental rifting, CO_2 degassing and climate change through time. *Nature Geoscience*, *10*(12), 941–946. https://doi.org/10.1038/s41561-017-0003-6

Budnik, R. T. (1986). Left-lateral intraplate deformation along the Ancestral Rocky Mountains: Implications for late Paleozoic plate motions. *Tectonophysics*, *132*(1–3), 195–214. https://doi.org/10.1016/0040-1951(86)90032-6

Caldwell, T. G., Bibby, H. M., & Brown, C. (2004). The magnetotelluric phase tensor. *Geophysical Journal International*, *158*(2), 457–469. https://doi.org/10.1111/j.1365-246X.2004.02281.x

Chang, W. F., McMechan, G. A., & Keller, G. R. (1989). Wave field processing of data from a large-aperture seismic experiment in southwestern Oklahoma. *Journal of Geophysical Research*, *94*(B2), 1803–1816. https://doi.org/10.1029/JB094iB02p01803

Chase, B. F., Kolawole, F., Atekwana, E. A., Carpenter, B. M., Turko, M., Abdelsalam, M., & Finn, C. (2022). The 180-km-long Meers-Willow fault system in the Southern Oklahoma Aulacogen: A potential US mid-continent seismic hazard. *GSA Bulletin*, *135*(3–4), 663–677. https://doi.org/10.1130/B36363.1

Chave, A. D., & Thomson, D. J. (2004). Bounded influence magnetotelluric response function estimation. *Geophysical Journal International*, *157*(3), 988–1006. https://doi.org/10.1111/j.1365-246X.2004.02203.x

Chen, L. (2017). Layering of subcontinental lithospheric mantle. *Science Bulletin*, *62*(14), 1030–1034. https://doi.org/10.1016/j.scib.2017.06.003

Clemens, J. D., Holloway, J. R., & White, A. J. R. (1986). Origin of an A-type granite; experimental constraints. *American Mineralogist*, *71*(3–4), 317–324.

Comiskey, C. (2013). Seismic anisotropy in Texas and Oklahoma and its relationship to tectonic events that shaped Southern Laurentia. (Doctoral dissertation).

Craddock, J. P., Jackson, M., van der Pluijm, B. A., & Versical, R. T. (1993). Regional shortening fabrics in eastern North America: Far-field stress transmission from the Appalachian-Ouachita Orogenic Belt. *Tectonics*, *12*(1), 257–264. https://doi.org/10.1029/92TC01106

Dall'Agnol, R., Scaillet, B., & Pichavant, M. (1999). An experimental study of a lower Proterozoic A-type granite from the Eastern Amazonian Craton, Brazil. *Journal of Petrology*, *40*(11), 1673–1698. https://doi.org/10.1093/petroj/40.11.1673

Dasgupta, R., & Hirschmann, M. M. (2010). The deep carbon cycle and melting in Earth's interior. *Earth and Planetary Science Letters*, *298*(1–2), 1–13. https://doi.org/10.1016/j.epsl.2010.06.039

Davis, H. G., Northcutt, R. A., & Johnson, K. S. (1988). The greater Anadarko Basin: An overview of petroleum exploration and development. In *Anadarko basin symposium* (pp. 13–24).

Deen, T. J., Griffin, W. L., Begg, G., O'Reilly, S. Y., Natapov, L. M., & Hronsky, J. (2006). Thermal and compositional structure of the subcontinental lithospheric mantle: Derivation from shear wave seismic tomography. *Geochemistry, Geophysics, Geosystems*, *7*(7), Q07003. https://doi.org/10.1029/2005GC001120

De Hoog, J. C., Gall, L., & Cornell, D. H. (2010). Trace-element geochemistry of mantle olivine and application to mantle petrogenesis and geothermobarometry. *Chemical Geology*, *270*(1–4), 196–215. https://doi.org/10.1016/j.chemgeo.2009.11.017

DeLucia, M. S., Murphy, B. S., Marshak, S., & Egbert, G. D. (2019). The Missouri High-Conductivity Belt, revealed by magnetotelluric imaging: Evidence of a trans-lithospheric shear zone beneath the Ozark Plateau, Midcontinent USA? *Tectonophysics*, *753*, 111–123. https://doi.org/10.1016/j.tecto.2019.01.011

Duba, A. G., & Shankland, T. J. (1982). Free carbon & electrical conductivity in the Earth's mantle. *Geophysical Research Letters*, *9*(11), 1271–1274. https://doi.org/10.1029/GL009i011p01271

Evanzia, D., Pulliam, J., Ainsworth, R., Gurrola, H., & Pratt, K. (2014). Seismic Vp & Vs tomography of Texas & Oklahoma with a focus on the Gulf Coast margin. *Earth and Planetary Science Letters*, *402*, 148–156. https://doi.org/10.1016/j.epsl.2013.12.027

Faul, U. H., Cline, C. J., II, David, E. C., Berry, A. J., & Jackson, I. (2016). Titanium-hydroxyl defect-controlled rheology of the Earth's upper mantle. *Earth and Planetary Science Letters*, *452*, 227–237. https://doi.org/10.1016/j.epsl.2016.07.016

Fei, H., Wiedenbeck, M., Yamazaki, D., & Katsura, T. (2013). Small effect of water on upper-mantle rheology based on silicon self-diffusion coefficients. *Nature*, *498*(7453), 213–215. https://doi.org/10.1038/nature12193

Foley, S. (1992). Vein-plus-wall-rock melting mechanisms in the lithosphere and the origin of potassic alkaline magmas. *Lithos*, *28*(3–6), 435–453. https://doi.org/10.1016/0024-4937(92)90018-T

Foley, S. F. (2008). Rejuvenation and erosion of the cratonic lithosphere. *Nature Geoscience*, *1*(8), 503–510. https://doi.org/10.1038/ngeo261

Foley, S. F., & Fischer, T. P. (2017). An essential role for continental rifts and lithosphere in the deep carbon cycle. *Nature Geoscience*, *10*(12), 897–902. https://doi.org/10.1038/s41561-017-0002-7

Forst, B. R., & Lindsley, D. H. (1992). Equilibria among Fe-Ti oxides, pyroxenes, olivine, and quartz: Part II. Application. *American Mineralogist*, *77*(9–10), 1004–1020.

Frezzotti, M. L., & Ferrando, S. (2018). The role of halogens in the lithospheric mantle. *The Role of Halogens in Terrestrial and Extraterrestrial Geochemical Processes: Surface, Crust, and Mantle*, 805–845. https://doi.org/10.1007/978-3-319-61667-4_13

Frost, D. J. (2006). The stability of hydrous mantle phases. *Reviews in Mineralogy and Geochemistry*, *62*(1), 243–271. https://doi.org/10.2138/rmg.2006.62.11

Gardés, E., Gaillard, F., & Tarits, P. (2014). Toward a unified hydrous olivine electrical conductivity law. *Geochemistry, Geophysics, Geosystems*, *15*(12), 4984–5000. https://doi.org/10.1002/2014GC005496

Gaudemer, Y., Jaupart, C., & Tapponnier, P. (1988). Thermal control on post-orogenic extension in collision belts. *Earth and Planetary Science Letters*, *89*(1), 48–62. https://doi.org/10.1016/0012-821X(88)90032-5

Gilbert, M. C. (1983). Timing and chemistry of igneous events associated with the southern Oklahoma aulacogen. In *Developments in geotectonics* (Vol. 19, pp. 439–455). Elsevier. https://doi.org/10.1016/B978-0-444-42198-2.50030-4

Glover, P. W. (2010). A generalized Archie's law for *n* phases. *Geophysics*, *75*(6), E247–E265. https://doi.org/10.1190/1.3509781

Glover, P. W., & Ádám, A. (2008). Correlation between crustal high conductivity zones and seismic activity and the role of carbon during shear deformation. *Journal of Geophysical Research*, *113*(B12), B12210. https://doi.org/10.1029/2008JB005804

Godel, B., Barnes, S. J., & Maier, W. D. (2006). 3-D distribution of sulphide minerals in the Merensky Reef (Bushveld Complex, South Africa) and the JM Reef (Stillwater Complex, USA) and their relationship to microstructures using X-ray computed tomography. *Journal of Petrology*, *47*(9), 1853–1872. https://doi.org/10.1093/petrology/egl029

Granath, J. W. (1989). Structural evolution of the Ardmore Basin, Oklahoma: Progressive deformation in the foreland of the Ouachita collision. *Tectonics*, *8*(5), 1015–1036. https://doi.org/10.1029/TC008i005p01015

Green, D. H., & Ringwood, A. E. (1967). The Genesis of basaltic magmas. *Contributions to Mineralogy and Petrology*, *15*(2), 103–190. https://doi.org/10.1007/BF00372052

Green, J. C., & Fitz, T. J., III. (1993). Extensive felsic lavas and rheoignimbrites in the Keweenawan Midcontinent Rift plateau volcanics, Minnesota: Petrographic and field recognition. *Journal of Volcanology and Geothermal Research*, *54*(3–4), 177–196. https://doi.org/10.1016/0377-0273(93)90063-W

Grégoire, M., Bell, D., & Le Roex, A. (2002). Trace element geochemistry of phlogopite-rich mafic mantle xenoliths: Their classification and their relationship to phlogopite-bearing peridotites and kimberlites revisited. *Contributions to Mineralogy and Petrology*, *142*(5), 603–625. https://doi.org/10.1007/s00410-001-0315-8

Griffin, W. L., Begg, G. C., Dunn, D., O'Reilly, S. Y., Natapov, L. M., & Karlstrom, K. (2011). Archean lithospheric mantle beneath Arkansas: Continental growth by microcontinent accretion. *Bulletin*, *123*(9–10), 1763–1775. https://doi.org/10.1130/B30253.1

Griffin, W. L., Begg, G. C., & O'reilly, S. Y. (2013). Continental-root control on the Genesis of magmatic ore deposits. *Nature Geoscience*, *6*(11), 905–910. https://doi.org/10.1038/ngeo1954

Griffin, W. L., O'Reilly, S. Y., Afonso, J. C., & Begg, G. C. (2009). The composition and evolution of lithospheric mantle: A re-evaluation and its tectonic implications. *Journal of Petrology*, *50*(7), 1185–1204. https://doi.org/10.1093/petrology/egn033

Griffin, W. L., O'Reilly, S. Y., Doyle, B. J., Pearson, N. J., Coopersmith, H., Kivi, K., et al. (2004). Lithosphere mapping beneath the North American plate. *Lithos*, *77*(1–4), 873–922. https://doi.org/10.1016/j.lithos.2004.03.034

Ham, W. E., Denison, R. E., & Merritt, C. A. (1964). Basement rocks and structural evolution of southern Oklahoma. *AAPG Bulletin*, *48*(4), 529. https://doi.org/10.1306/BC743C77-16BE-11D7-8645000102C1865D

Hansen, S. M., Dueker, K., & Schmandt, B. (2015). Thermal classification of lithospheric discontinuities beneath USArray. *Earth and Planetary Science Letters*, *431*, 36–47. https://doi.org/10.1016/j.epsl.2015.09.009

Hanson, R. E., Puckett, R. E., Jr., Keller, G. R., Brueseke, M. E., Bulen, C. L., Mertzman, S. A., et al. (2013). Intraplate magmatism related to opening of the southern Iapetus Ocean: Cambrian Wichita igneous province in the Southern Oklahoma rift zone. *Lithos*, *174*, 57–70. https://doi.org/10.1016/j.lithos.2012.06.003

Hasterok, D., & Chapman, D. S. (2011). Heat production and geotherms for the continental lithosphere. *Earth and Planetary Science Letters*, *307*(1–2), 59–70. https://doi.org/10.1016/j.epsl.2011.04.034

Hirschmann, M. M., Tenner, T., Aubaud, C., & Withers, A. C. (2009). Dehydration melting of nominally anhydrous mantle: The primacy of partitioning. *Physics of the Earth and Planetary Interiors*, *176*(1–2), 54–68. https://doi.org/10.1016/j.pepi.2009.04.001

Hirth, G., & Kohlstedt, D. L. (1996). Water in the oceanic upper mantle: Implications for rheology, melt extraction and the evolution of the lithosphere. *Earth and Planetary Science Letters*, *144*(1–2), 93–108. https://doi.org/10.1016/0012-821x(96)00154-9

Hoffman, P., Dewey, J. F., & Burke, K. (1974). *Aulacogens and their genetic relation to geosynclines, with a Proterozoic example from Great Slave Lake*. Canada. https://doi.org/10.2110/pec.74.19.0038

Hofmann, A. W. (1997). Mantle geochemistry: The message from oceanic volcanism. *Nature*, *385*(6613), 219–229. https://doi.org/10.1038/385219a0

Hogan, J. P., & Gilbert, M. C. (1995). The A-type Mount Scott Granite sheet: Importance of crystal magma traps. *Journal of Geophysical Research*, *100*(B8), 15779–15792. https://doi.org/10.1029/94JB03258

Hogan, J. P., & Gilbert, M. C. (1998). The Southern Oklahoma aulacogen: A Cambrian analog for Mid-Proterozoic AMCG (anorthosite -mangerite-charnockite-granite) complexes? *Basement Tectonics 12: Central North America and Other Regions*, 39–78. https://doi.org/10.1007/978-94-011-5098-9_3

Hornsby, K. T., Streig, A. R., Bennett, S. E., Chang, J. C., & Mahan, S. (2020). Neotectonic and paleoseismic analysis of the northwest extent of Holocene surface deformation along the Meers Fault, Oklahoma. *Bulletin of the Seismological Society of America*, *110*(1), 49–66. https://doi.org/10.1785/0120180148

Hu, H., Dai, L., Li, H., Sun, W., & Li, B. (2018). Effect of dehydrogenation on the electrical conductivity of Fe-bearing amphibole: Implications for high conductivity anomalies in subduction zones and continental crust. *Earth and Planetary Science Letters*, *498*, 27–37. https://doi.org/10.1016/j.epsl.2018.06.003

Hu, J., Liu, L., Faccenda, M., Zhou, Q., Fischer, K. M., Marshak, S., & Lundstrom, C. (2018). Modification of the Western Gondwana craton by plume–lithosphere interaction. *Nature Geoscience*, *11*(3), 203–210. https://doi.org/10.1038/s41561-018-0064-1

Joachim, B., Stechern, A., Ludwig, T., Konzett, J., Pawley, A., Ruzié-Hamilton, L., et al. (2017). Effect of water on the fluorine and chlorine partitioning behavior between olivine and silicate melt. *Contributions to Mineralogy and Petrology*, *172*(4), 1–15. https://doi.org/10.1007/s00410-017-1329-1

Jones, A. G., Ledo, J., & Ferguson, I. J. (2005). Electromagnetic images of the Trans-Hudson orogen: The North American Central Plains anomaly revealed. *Canadian Journal of Earth Sciences*, *42*(4), 457–478. https://doi.org/10.1139/e05-018

Jones, M. T., Jerram, D. A., Svensen, H. H., & Grove, C. (2016). The effects of large igneous provinces on the global carbon and sulphur cycles. *Palaeogeography, Palaeoclimatology, Palaeoecology*, *441*, 4–21. https://doi.org/10.1016/j.palaeo.2015.06.042

Kaminski, E., & Jaupart, C. (2000). Lithosphere structure beneath the Phanerozoic intracratonic basins of North America. *Earth and Planetary Science Letters*, *178*(1–2), 139–149. https://doi.org/10.1016/S0012-821X(00)00067-4

Keller, G. R., & Baldridge, W. S. (2006). The southern Oklahoma aulacogen. In *Developments in geotectonics* (Vol. 25, pp. 427–436). Elsevier. https://doi.org/10.1016/S0419-0254(06)80020-0

Keller, G. R., Braile, L. W., McMechan, G. A., Thomas, W. A., Harder, S. H., Chang, W. F., & Jardine, W. G. (1989). Paleozoic continent-ocean transition in the Ouachita Mountains imaged from PASSCAL wide-angle seismic reflection-refraction data. *Geology*, *17*(2), 119–122. https://doi.org/10.1130/0091-7613(1989)017<0119:PCOTIT>2.3.CO;2

Keller, G. R., & Stephenson, R. A. (2007). The southern Oklahoma and Dniepr-Donets aulacogens: A comparative analysis.

Klimm, K., Holtz, F., Johannes, W., & King, P. L. (2003). Fractionation of metaluminous A-type granites: An experimental study of the Wangrah Suite, Lachlan Fold Belt, Australia. *Precambrian Research*, *124*(2–4), 327–341. https://doi.org/10.1016/S0301-9268(03)00092-5

Kluth, C. F., & Coney, P. J. (1981). Plate tectonics of the ancestral Rocky Mountains. *Geology*, *9*(1), 10–15. https://doi.org/10.1130/0091-7613(1981)9<10:PTOTAR>2.0.CO;2

Kumar, P., Kind, R., Yuan, X., & Mechie, J. (2012). USArray receiver function images of the lithosphere-asthenosphere boundary. *Seismological Research Letters*, *83*(3), 486–491. https://doi.org/10.5194/se-3-149-2012

Laske, G., Masters, G., Ma, Z., & Pasyanos, M. (2013). Update on CRUST1. 0—A 1-degree global model of Earth's crust. *EGU General Assembly Geophysicla Research Abstracts*, *15*(3), 2658.

Leary, R. J., Umhoefer, P., Smith, M. E., & Riggs, N. (2017). A three-sided orogen: A new tectonic model for Ancestral Rocky Mountain uplift and basin development. *Geology*, *45*(8), 735–738. https://doi.org/10.1130/G39041.1

Lee, C. T. A., Luffi, P., & Chin, E. J. (2011). Building and destroying continental mantle. *Annual Review of Earth and Planetary Sciences*, *39*(1), 59–90. https://doi.org/10.1146/annurev-earth-040610-133505

Li, Y., Jiang, H., & Yang, X. (2017). Fluorine follows water: Effect on electrical conductivity of silicate minerals by experimental constraints from phlogopite. *Geochimica et Cosmochimica Acta*, *217*, 16–27. https://doi.org/10.1016/j.gca.2017.08.020

Li, Y., Yang, X., Yu, J. H., & Cai, Y. F. (2016). Unusually high electrical conductivity of phlogopite: The possible role of fluorine and geophysical implications. *Contributions to Mineralogy and Petrology*, *171*(4), 1–11. https://doi.org/10.1007/s00410-016-1252-x

Lidiak, E. G., Denison, R. E., & Stern, R. J. (2014). Cambrian (?) mill creek diabase dike swarm, Eastern arbuckles: A glimpse of Cambrian rifting in the southern Oklahoma aulacogen. *Oklahoma Geological Survey, Guidebook*, *38*, 105–122.

Liu, J., Pearson, D. G., Wang, L. H., Mather, K. A., Kjarsgaard, B. A., Schaeffer, A. J., et al. (2021). Plume-driven recratonization of deep continental lithospheric mantle. *Nature*, *592*(7856), 732–736. https://doi.org/10.6084/m9.figshare.13789354

Mandler, B. E., & Grove, T. L. (2016). Controls on the stability and composition of amphibole in the Earth's mantle. *Contributions to Mineralogy and Petrology*, *171*(8–9), 1–20. https://doi.org/10.1007/s00410-016-1281-5

Marsh, S., & Holland, A. (2016). *Comprehensive fault database and interpretive fault map of Oklahoma*. Oklahoma Geol. Surv. Open-File Rep. OF2-2016. Oklahoma Geological Survey.

Marshak, S., Nelson, W. J., & McBride, J. H. (2003). Phanerozoic strike-slip faulting in the continental interior platform of the United States: Examples from the Laramide Orogen, midcontinent, and ancestral Rocky Mountains. *Geological Society, London, Special Publications*, *210*(1), 159–184. https://doi.org/10.1144/GSL.SP.2003.210.01.10

Martí, A. (2014). The role of electrical anisotropy in magnetotelluric responses: From modelling and dimensionality analysis to inversion and interpretation. *Surveys in Geophysics*, *35*(1), 179–218. https://doi.org/10.1007/s10712-013-9233-3

Martin, R. F. (2006). A-type granites of crustal origin ultimately result from open-system fenitization-type reactions in an extensional environment. *Lithos*, *91*(1–4), 125–136. https://doi.org/10.1016/j.lithos.2006.03.012

Mathez, E. A. (1987). Carbonaceous matter in mantle xenoliths: Composition and relevance to the isotopes. *Geochimica et Cosmochimica Acta*, *51*(9), 2339–2347. https://doi.org/10.1016/0016-7037(87)90288-2

Mathez, E. A., Dietrich, V. J., & Irving, A. J. (1984). The geochemistry of carbon in mantle peridotites. *Geochimica et Cosmochimica Acta*, *48*(9), 1849–1859. https://doi.org/10.1016/0016-7037(84)90038-3

McConnell, D. A. (1989). Determination of offset across the northern margin of the Wichita uplift, southwest Oklahoma. *Geological Society of America Bulletin*, *101*(10), 1317–1332. https://doi.org/10.1130/0016-7606(1989)101<1317:DOOATN>2.3.CO;2

McConnell, D. A., & Gilbert, M. C. (1990). Cambrian extensional tectonics and magmatism within the Southern Oklahoma aulacogen. *Tectonophysics*, *174*(1–2), 147–157. https://doi.org/10.1016/0040-1951(90)90388-O

McKenzie, D. (1985). The extraction of magma from the crust and mantle. *Earth and Planetary Science Letters*, *74*(1), 81–91. https://doi.org/10.1016/0012-821X(85)90168-2

Miller, J. D., Nicholson, S. W., Easton, R. M., Ripley, E. M., & Feinberg, J. M. (2013). Geology and mineral deposits of the 1.1 Ga Midcontinent Rift in the Lake Superior region—An overview. In J. Miller (Ed.), *Field guide to the copper-nickel-platinum group element deposits of the Lake Superior Region* (Vol. 13, No. (1), pp. 1–49). Precambrian Research Center Guidebook.

Murphy, B. S., Huizenga, J. M., & Bedrosian, P. A. (2022). Graphite as an electrically conductive indicator of ancient crustal-scale fluid flow within mineral systems. *Earth and Planetary Science Letters*, *594*, 117700. https://doi.org/10.1016/j.epsl.2022.117700

Naif, S. (2018). An upper bound on the electrical conductivity of hydrated oceanic mantle at the onset of dehydration melting. *Earth and Planetary Science Letters*, *482*, 357–366. https://doi.org/10.1016/j.epsl.2017.11.024

Netto, A., & Pulliam, J. (2020). Upper mantle structure of the southern US continental margin from teleseismic traveltime tomography. *Geophysical Research Letters*, *47*(7), e2019GL085482. https://doi.org/10.1029/2019GL085482

Nyamwandha, C. A., Powell, C. A., & Langston, C. A. (2016). A joint local and teleseismic tomography study of the Mississippi Embayment and New Madrid Seismic Zone. *Journal of Geophysical Research: Solid Earth*, *121*(5), 3570–3585. https://doi.org/10.1002/2015JB012761

Nyblade, A. A., & Brazier, R. A. (2002). Precambrian lithospheric controls on the development of the East African rift system. *Geology*, *30*(8), 755–758. https://doi.org/10.1130/0091-7613(2002)030<0755:PLCOTD>2.0.CO;2

O'Reilly, S. Y., & Griffin, W. L. (2013). Mantle metasomatism. *Metasomatism and the chemical transformation of rock*, 471–533. https://doi.org/10.1007/978-3-642-28394-9_12

Özaydın, S., & Selway, K. (2020). MATE: An analysis tool for the interpretation of magnetotelluric models of the mantle. *Geochemistry, Geophysics, Geosystems*, *21*(9), e2020GC009126. https://doi.org/10.1029/2020GC009126

Özaydın, S., & Selway, K. (2022). The relationship between kimberlitic magmatism and electrical conductivity anomalies in the mantle. *Geophysical Research Letters*, *49*(18), e2022GL099661. https://doi.org/10.1029/2022GL099661

Özaydın, S., Selway, K., Griffin, W. L., & Moorkamp, M. (2022). Probing the southern African lithosphere with magnetotellurics: 2. Linking electrical conductivity, composition, and tectonomagmatic evolution. *Journal of Geophysical Research: Solid Earth*, *127*(3), e2021JB023105. https://doi.org/10.1029/2021JB023105

Padrón-Navarta, J. A., & Hermann, J. (2017). A subsolidus olivine water solubility equation for the Earth's upper mantle. *Journal of Geophysical Research: Solid Earth*, *122*(12), 9862–9880. https://doi.org/10.1002/2017JB014510

Parkinson, W. D. (1959). Directions of rapid geomagnetic fluctuations. *Geophysical Journal International*, *2*(1), 1–14. https://doi.org/10.1111/j.1365-246X.1959.tb05776.x

Pearson, D. G., & Wittig, N. (2014). The formation and evolution of cratonic mantle lithosphere—Evidence from mantle xenoliths. In K. K. Turekian & H. D. Holland (Eds.), *Treatise on geochemistry* (pp. 255–92).

Perry, W. J. (1989). *Tectonic evolution of the Anadarko basin region, Oklahoma*. (No. 1866). Department of the Interior, US Geological Survey.

Peslier, A. H., Woodland, A. B., Bell, D. R., & Lazarov, M. (2010). Olivine water contents in the continental lithosphere and the longevity of cratons. *Nature*, *467*(7311), 78–81. https://doi.org/10.1038/nature09317

Pineau, F., & Mathez, E. A. (1990). Carbon isotopes in xenoliths from the Hualalai Volcano, Hawaii, and the generation of isotopic variability. *Geochimica et Cosmochimica Acta*, *54*(1), 217–227. https://doi.org/10.1016/0016-7037(90)90209-4

Pommier, A., Kohlstedt, D. L., Hansen, L. N., Mackwell, S., Tasaka, M., Heidelbach, F., & Leinenweber, K. (2018). Transport properties of olivine grain boundaries from electrical conductivity experiments. *Contributions to Mineralogy and Petrology*, *173*(5), 1–13. https://doi.org/10.1007/s00410-018-1468-z

Porritt, R. W., Allen, R. M., & Pollitz, F. F. (2014). Seismic imaging east of the Rocky Mountains with USArray. *Earth and Planetary Science Letters*, *402*, 16–25. https://doi.org/10.1016/j.epsl.2013.10.034

Powell, B. N., & Phelps, D. W. (1977). Igneous cumulates of the Wichita province and their tectonic implications. *Geology*, *5*(1), 52–56. https://doi.org/10.1130/0091-7613(1977)5<52:icotwp>2.0.co;2

Pratt, T. L., Hauser, E. C., & Nelson, K. D. (1992). Widespread buried Precambrian layered sequences in the US mid-continent: Evidence for large Proterozoic depositional basins. *AAPG Bulletin*, *76*(9), 1384–1401. https://doi.org/10.1306/BDFF89FC-1718-11D7-8645000102C1865D

Price, J. D. (2014). The Mount Scott intrusive suite, Wichita Mountains, Oklahoma. *Oklahoma Geological Survey Guidebook*, *38*, 299–318.

Price, J. D., Hogan, J. P., Gilbert, M. C., London, D., & Morgan, G. B. (1999). Experimental study of titanite-fluorite equilibria in the A-type Mount Scott Granite: Implications for assessing F contents of felsic magma. *Geology*, *27*(10), 951–954. https://doi.org/10.1130/0091-7613(1999)027<0951:ESOTFE>2.3.CO;2

Priestley, K., McKenzie, D., & Ho, T. (2018). A lithosphere–asthenosphere boundary—A global model derived from multimode surface-wave tomography and petrology. *Lithospheric Discontinuities*, 111–123. https://doi.org/10.1002/9781119249740.ch6

Puckett, R. E., Hanson, R. E., Eschberger, A. M., Brueseke, M. E., Bulen, C. L., Price, J. D., & Suneson, N. (2014). New insights into the early Cambrian igneous and sedimentary history of the Arbuckle Mountains area of the Southern Oklahoma aulacogen from basement well penetrations. In *Igneous and tectonic history of the southern Oklahoma Aulacogen38* (pp. 61–94).

Puelles, P., Ábalos, B., & Fernández-Armas, S. (2014). Graphite and quartz petrofabrics: Examples from the Ediacaran black quartzites of the Ossa-Morena Zone (SW Iberia). *Tectonophysics*, *615*, 53–68. https://doi.org/10.1016/j.tecto.2013.12.018

Rader, E., Emry, E., Schmerr, N., Frost, D., Cheng, C., Menard, J., et al. (2015). Characterization and petrological constraints of the midlithospheric discontinuity. *Geochemistry, Geophysics, Geosystems*, *16*(10), 3484–3504. https://doi.org/10.1002/2015GC005943

Refayee, H. A., Yang, B. B., Liu, K. H., & Gao, S. S. (2014). Mantle flow and lithosphere–asthenosphere coupling beneath the southwestern edge of the North American craton: Constraints from shear-wave splitting measurements. *Earth and Planetary Science Letters*, *402*, 209–220. https://doi.org/10.1016/j.epsl.2013.01.031

Rehfeldt, T., Foley, S. F., Jacob, D. E., Carlson, R. W., & Lowry, D. (2008). Contrasting types of metasomatism in dunite, wehrlite and websterite xenoliths from Kimberley, South Africa. *Geochimica et Cosmochimica Acta*, *72*(23), 5722–5756. https://doi.org/10.1016/j.gca.2008.08.020

Rodi, W., & Mackie, R. L. (2001). Nonlinear conjugate gradients algorithm for 2-D magnetotelluric inversion. *Geophysics*, *66*(1), 174–187. https://doi.org/10.1190/1.1444893

Rychert, C. A., Shearer, P. M., & Fischer, K. M. (2010). Scattered wave imaging of the lithosphere–asthenosphere boundary. *Lithos*, *120*(1–2), 173–185. https://doi.org/10.1016/j.lithos.2009.12.006

Safonov, O., Butvina, V., & Limanov, E. (2019). Phlogopite-forming reactions as indicators of metasomatism in the lithospheric mantle. *Minerals*, *9*(11), 685. https://doi.org/10.3390/min9110685

Salters, V. J., Longhi, J. E., & Bizimis, M. (2002). Near mantle solidus trace element partitioning at pressures up to 3.4 GPa. *Geochemistry, Geophysics, Geosystems*, *3*(7), 1–23. https://doi.org/10.1029/2001GC000148

Saxena, S., Pommier, A., & Tauber, M. J. (2021). Iron sulfides and anomalous electrical resistivity in cratonic environments. *Journal of Geophysical Research: Solid Earth*, *126*(9), e2021JB022297. https://doi.org/10.1029/2021JB022297

Selway, K. (2014). On the causes of electrical conductivity anomalies in tectonically stable lithosphere. *Surveys in Geophysics*, *35*(1), 219–257. https://doi.org/10.1007/s10712-013-9235-1

Selway, K. (2018). Electrical discontinuities in the continental lithosphere imaged with magnetotellurics. *Lithospheric Discontinuities*, 89–109. https://doi.org/10.1002/9781119249740.ch5

Selway, K., Ford, H., & Kelemen, P. (2015). The seismic mid-lithosphere discontinuity. *Earth and Planetary Science Letters*, *414*, 45–57. https://doi.org/10.1016/j.epsl.2014.12.029

Shen, W., Ritzwoller, M. H., & Schulte-Pelkum, V. (2013). Crustal and uppermost mantle structure in the central US encompassing the Midcontinent Rift. *Journal of Geophysical Research: Solid Earth*, *118*(8), 4325–4344. https://doi.org/10.1002/jgrb.50321

Shirey, S. B., Berg, J. H., & Carlson, R. W. (1994). Temporal changes in the sources of flood basalts: Isotopic and trace element evidence from the 1100 Ma old Keweenawan Mamainse Point Formation, Ontario, Canada. *Geochimica et Cosmochimica Acta*, *58*(20), 4475–4490. https://doi.org/10.1016/0016-7037(94)90349-2

Skulski, T., Francis, D., & Ludden, J. (1991). Arc-transform magmatism in the Wrangell volcanic belt. *Geology*, *19*(1), 11–14. https://doi.org/10.1130/0091-7613(1991)019<0011:ATMITW>2.3.CO;2

Skulski, T., Francis, D., & Ludden, J. (1992). Volcanism in an arc-transform transition zone: The stratigraphy of the St.Clare creek volcanic field, Wrangell volcanic belt, Yukon, Canada. *Canadian Journal of Earth Sciences*, *29*(3), 446–461. https://doi.org/10.1139/e92-039

Smith, J. V. (1981). Halogen and phosphorus storage in the Earth. *Nature*, *289*(5800), 762–765. https://doi.org/10.1038/289762a0

Stachel, T., & Luth, R. W. (2015). Diamond formation—Where, when and how? *Lithos*, *220*, 200–220. https://doi.org/10.1016/j.lithos.2015.01.028

Stagno, V., & Frost, D. J. (2010). Carbon speciation in the asthenosphere: Experimental measurements of the redox conditions at which carbonate-bearing melts coexist with graphite or diamond in peridotite assemblages. *Earth and Planetary Science Letters*, *300*(1–2), 72–84. https://doi.org/10.1016/j.epsl.2010.09.038

Tang, Y. J., Zhang, H. F., Santosh, M., & Ying, J. F. (2013). Differential destruction of the North China craton: A tectonic perspective. *Journal of Asian Earth Sciences*, *78*, 71–82. https://doi.org/10.1016/j.jseaes.2012.11.047

Tave, M. A. (2013). Imaging of the crust and Moho beneath Oklahoma using receiver functions and Pn tomography; with emphasis on the Southern Oklahoma Aulacogen. (Doctoral dissertation).

Ten Grotenhuis, S. M., Drury, M. R., Peach, C. J., & Spiers, C. J. (2004). Electrical properties of fine-grained olivine: Evidence for grain boundary transport. *Journal of Geophysical Research*, *109*(B6), B06203. https://doi.org/10.1029/2003JB002799

Thomas, W. A. (2011). The Iapetan rifted margin of southern Laurentia. *Geosphere*, *7*(1), 97–120. https://doi.org/10.1130/GES00574.1

Thomas, W. A. (2014). The southern Oklahoma transform-parallel intracratonic fault system. *Oklahoma Geological Survey, Guidebook*, *38*, 375–388. Retrieved from http://ogs.ou.edu/docs/guidebooks/GB38PIIRP14.pdf

Turko, M., & Mitra, S. (2021). Structural geometry and evolution of the Carter-Knox structure, Anadarko Basin, Oklahoma. *AAPG Bulletin*, *105*(10), 1993–2015. https://doi.org/10.1306/08212019114

Vervoort, J. D., Wirth, K., Kennedy, B., Sandland, T., & Harpp, K. S. (2007). The magmatic evolution of the Midcontinent rift: New geochronologic and geochemical evidence from felsic magmatism. *Precambrian Research*, *157*(1–4), 235–268. https://doi.org/10.1016/j.precamres.2007.02.019

Vozoff, K. (1972). The magnetotelluric method in the exploration of sedimentary basins. *Geophysics*, *37*(1), 98–141. https://doi.org/10.1190/1.1440255

Wall, C. J., Hanson, R. E., Schmitz, M., Price, J. D., Donovan, R. N., Boro, J. R., et al. (2021). Integrating zircon trace-element geochemistry and high-precision U-Pb zircon geochronology to resolve the timing and petrogenesis of the late Ediacaran–Cambrian Wichita igneous province, Southern Oklahoma Aulacogen, USA. *Geology*, *49*(3), 268–272. https://doi.org/10.1130/G48140.1

Watson, E. B., & Brenan, J. M. (1987). Fluids in the lithosphere, 1. Experimentally-determined wetting characteristics of CO_2H_2O fluids and their implications for fluid transport, host-rock physical properties, and fluid inclusion formation. *Earth and Planetary Science Letters*, *85*(4), 497–515. https://doi.org/10.1016/0012-821X(87)90144-0

Whitmeyer, S. J., & Karlstrom, K. E. (2007). Tectonic model for the Proterozoic growth of North America. *Geosphere*, *3*(4), 220–259. https://doi.org/10.1130/GES00055.1

Wirth, E. A., & Long, M. D. (2014). A contrast in anisotropy across mid-lithospheric discontinuities beneath the central United States—A relic of craton formation. *Geology*, *42*(10), 851–854. https://doi.org/10.1130/g35804.1

Yang, B., Egbert, G. D., Kelbert, A., & Meqbel, N. M. (2015). Three-dimensional electrical resistivity of the north-central USA from EarthScope long period magnetotelluric data. *Earth and Planetary Science Letters*, *422*, 87–93. https://doi.org/10.1016/j.epsl.2015.04.006

Yoshino, T., & Noritake, F. (2011). Unstable graphite films on grain boundaries in crustal rocks. *Earth and Planetary Science Letters*, *306*(3–4), 186–192. https://doi.org/10.1016/j.epsl.2011.04.003

Yuan, H., French, S., Cupillard, P., & Romanowicz, B. (2014). Lithospheric expression of geological units in central and eastern North America from full waveform tomography. *Earth and Planetary Science Letters*, *402*, 176–186. https://doi.org/10.1016/j.epsl.2013.11.057

Yuan, H., & Romanowicz, B. (2010). Lithospheric layering in the North American craton. *Nature*, *466*(7310), 1063–1068. https://doi.org/10.1038/nature09332

Zhang, B., & Yoshino, T. (2017). Effect of graphite on the electrical conductivity of the lithospheric mantle. *Geochemistry, Geophysics, Geosystems*, *18*(1), 23–40. https://doi.org/10.1002/2016GC006530

Zientek, M. L. (2012). Magmatic ore deposits in layered intrusions - Descriptive model for reef-type PGE and contact-type Cu–Ni–PGE deposits. U.S. Geological Survey Open File. 2012-1010. Retrieved from https://pubs.usgs.gov/of/2012/1010/

References From the Supporting Information

Bell, D. R., Ihinger, P. D., & Rossman, G. R. (1995). Quantitative analysis of trace OH in garnet and pyroxenes. *American Mineralogist*, *80*(5–6), 465–474. https://doi.org/10.2138/am-1995-5-607

Dai, L., & Karato, S.-I. (2009a). Electrical conductivity of orthopyroxene: Implications for the water content of the asthenosphere. *Proceedings of the Japan Academy, Series B*, *85*(10), 466–475. https://doi.org/10.2183/pjab.85.466

Dai, L., & Karato, S.-I. (2009b). Electrical conductivity of pyrope-rich garnet at high temperature and high pressure. *Physics of the Earth and Planetary Interiors*, *176*(1–2), 83–88. https://doi.org/10.1016/j.pepi.2009.04.002

Demouchy, S., Shcheka, S., Denis, C. M. M., & Thoraval, C. (2017). Subsolidus hydrogen partitioning between nominally anhydrous minerals in garnet-bearing peridotite. *American Mineralogist*, *102*(9), 1822–1831. https://doi.org/10.2138/am-2017-6089

Foley, S. F., Prelevic, D., Rehfeldt, T., & Jacob, D. E. (2013). Minor and trace elements in olivines as probes into early igneous and mantle melting processes. *Earth and Planetary Science Letters*, *363*, 181–191. https://doi.org/10.1016/j.epsl.2012.11.025

Liu, H., Zhu, Q., & Yang, X. (2019). Electrical conductivity of OH-bearing omphacite and garnet in eclogite: The quantitative dependence on water content. *Contributions to Mineralogy and Petrology*, *174*(7), 1–15. https://doi.org/10.1007/s00410-019-1593-3

Novella, D., Frost, D. J., Hauri, E. H., Bureau, H., Raepsaet, C., & Roberge, M. (2014). The distribution of H_2O between silicate melt and nominally anhydrous peridotite and the onset of hydrous melting in the deep upper mantle. *Earth and Planetary Science Letters*, *400*, 1–13. https://doi.org/10.1016/j.epsl.2014.05.006

Withers, A. C., Bureau, H., Raepsaet, C., & Hirschmann, M. M. (2012). Calibration of infrared spectroscopy by elastic recoil detection analysis of H in synthetic olivine. *Chemical Geology*, *334*, 92–98. https://doi.org/10.1016/j.chemgeo.2012.10.002